

Aql X-1 from dawn 'til dusk: the early rise, fast state transition and decay of its 2024 outburst

A. Marino^{1,2,3}, F. Coti Zelati^{1,2,4}, K. Alabarta⁴, D. M. Russell⁵, Y. Cavecchi⁶, N. Rea^{1,2}, S. K. Rout⁵, T. Di Salvo⁷, J. Homan⁸, Á. Jurado-López¹, L. Ji⁹, R. Soria^{10,11,12}, T. D. Russell³, Y. L. Wang^{12,1,2,13}, A. Anita^{14,7}, M. C. Baglio⁴, H. Feng¹⁵, S. Fijma^{16,17}, S. Guillot¹⁸, Y. F. Huang^{19,20}, G. Illiano⁴, M. Imbrogno^{1,2}, C. Jin¹³, F. Lewis^{21,22}, Y. F. Liang^{23,24}, M. J. Liu¹³, R. Ma²⁵, G. Mastroserio²⁶, S. E. Motta⁴, J. U. Ness²⁷, E. Parent^{1,2}, A. Patruno^{1,2}, P. Saikia²⁸, L. Tao¹⁶, M. Veresvarska^{1,2}, X. P. Xu^{13,12}, W. Yuan^{13,12}, G. B. Zhang²⁹, Z. J. Zhang³⁰

(Affiliations can be found after the references)

XXX-XXX

ABSTRACT

Transient Low-Mass X-ray Binaries (LMXBs) are usually first detected by all-sky X-ray monitors when they enter new outbursts. These detections typically occur at X-ray luminosities above $\sim 10^{36}$ erg/s. As such, observations of these sources during the early rise of the outbursts have so far been very limited. However, the launch of the *Einstein Probe* (EP) has greatly improved our ability to detect fainter X-ray activity, unlocking access to the outburst early rise. In September 2024, EP detected the early onset of a new outburst from the well-known neutron star LMXB Aql X-1, catching the source at a luminosity below 10^{35} erg/s. In this paper we present results from a comprehensive, multi-wavelength campaign of this event, combining data from EP, *NICER*, *NuSTAR*, *Swift* and Las Cumbres Observatory covering the full outburst from its early rise through its return to quiescence. By comparing X-ray and optical light curves obtained with Las Cumbres Observatory during the initial rise, we show that the start of the X-ray emission lagged the optical rise by, at most, 3 days. Time-resolved X-ray spectroscopy revealed how the geometry and the physical properties of the accretion flow evolve during this early stage of the outburst, as well as at higher luminosities as the source transitioned through the canonical X-ray spectral states - hard, intermediate and soft. These data show that the source underwent a very rapid, about 12-h long, transition from the hard state to the soft state about two weeks after the optical onset of the outburst. The evolution of the temperature and physical sizes of both the inner region of the disk and a black body near the NS surface suggest that at the state transition, a boundary and spreading layer likely formed. We discuss these results in the context of time-scales for outburst evolution and state transitions in accreting neutron stars and black holes.

Key words. Stars: neutron – accretion, accretion disks – X-rays: binaries – X-rays: individual: Aql X-1

e-mail: marino@ice.csic.es

1. Introduction

Low-mass X-ray binaries (LMXBs) are binary systems composed of a black hole (BH) or a neutron star (NS) in orbit with a companion star of mass typically $\lesssim 1 M_{\odot}$ (Bahramian & De Genaar 2023). The electromagnetic output from these objects is powered by accretion of matter transferred from the companion star onto the compact object in the form of an accretion disk. The disk emission comprises a wide range of wavelengths, from near-IR and optical (originating in the outer disk) to hard X-rays, at hundreds of keVs (coming from the innermost region of the accretion flow). During their weeks-to-months long transient outbursts, LMXBs in outburst brighten by several orders of magnitude at all wavelengths. In particular, the X-ray luminosity can reach values close to the Eddington limit, attaining levels around 10^{38} – 10^{39} erg/s. Outside of these episodes, LMXBs are thought to reside in a regime called quiescence at X-ray luminosities below 10^{33} erg/s, where accretion onto the compact object proceeds at a much slower rate. Outbursts have been studied in detail from both an X-ray spectral and timing point of view, providing insights into how the geometry and the physical properties of the accretion flow change over time. Typically, three main components can be identified in the X-ray spectra of LMXBs (Lin et al. 2007; Di Salvo et al. 2023): a multi-color disk blackbody

originating from the inner regions of the disk; a Comptonization component characterized by power-law index Γ of ~ 1.5 – 3.0 and energy cut-off in the range 1–100 keV or sometimes above and originating from an optically thin hot corona; and a reflection spectrum (e.g. Fabian et al. 1989) due to the reprocessing of the emission from the corona by the disk. In accreting NSs, an additional blackbody component can be emitted from either the NS surface or a boundary layer (BL) in between the inner disk and the compact object (e.g. Inogamov & Sunyaev 1999; Babkovskaia et al. 2008; Suleimanov & Poutanen 2006; Marino et al. 2023). Depending on the broadband spectral shape, three main spectral states can be identified in LMXBs: a hard state, with emission dominated by the Comptonization component, a soft state, dominated by the disk (and/or the NS/BL components in NS LMXBs) and an intermediate state in between the two. The origin of these states has been historically associated to different stages of truncation of the optically thick disk (e.g. Esin et al. 1997), with the hard state being the regime where the disk is truncated furthest from the compact object (see, e.g. Zdziarski & De Marco 2020, and references therein for the debate regarding this model).

As they evolve through outburst, LMXBs often exhibit all three states in a hysteresis cycle from hard to intermediate to soft state and then backwards (e.g. Homan et al. 2001; Fender & Belloni 2004; Dunn et al. 2010; Marcel et al. 2018). When plotted in a Hardness Intensity Diagram (HID), these sources typically trace

a q-shaped track, so that these spectral states cycles are typically dubbed "q-tracks" or "q-diagrams" (e.g. Miyamoto et al. 1995; Zdziarski et al. 2004; Fender & Belloni 2004; Fender et al. 2009). While q-tracks are observed in both BH and NS LMXBs, the two classes of sources occasionally show markedly distinct behaviors; while BH sources generally perform horizontal hard-to-soft transition over time-scales of weeks (remaining at an approximately constant X-ray luminosity, e.g. Tetarenko et al. 2016), in NS LMXBs these transitions are diagonal, entailing a rise in X-ray luminosity, and occur rapidly, over time-scales of days (e.g. Muñoz-Darias et al. 2014; Marino et al. 2019). Similarly to the energy spectra, the observed X-ray Fourier power density spectra show a dramatic evolution throughout the q-track, with strong broadband noise only in the hard state and a significant drop of X-ray variability as the source moves to softer states (see, e.g., van der Klis 2004). However, the picture painted above describes only the evolution of LMXBs at luminosities above 1% of the Eddington limit, i.e., when they reach an X-ray luminosity of $\gtrsim 10^{36}$ erg/s. The early rise of an outburst, where systems brighten from quiescence, can be considered as an uncharted regime due to the limitations of current all-sky monitors. Past and present all-sky X-ray monitors, such as those on board the *Rossi X-ray Timing Explorer*, the *Monitor of All-sky X-ray Image* (MAXI/GSC), and the *Neil Gehrels Swift Observatory*, have not been sensitive enough to catch new X-ray activity unless it reached a triggering luminosity of about 3×10^{36} erg/s for Galactic sources, i.e., when the source had already entered the outburst phase completely. The early study of LMXB outbursts has so far significantly relied on continuous monitoring through ground-based optical telescopes, in particular through the program X-ray Binary New Early Warning System (XB-NEWS Russell et al. 2019) and similar efforts (e.g. Hameury et al. 1997; Jain et al. 2001; Buxton & Bailyn 2004). Due to these observational limitations, the physical mechanism responsible for triggering an outburst remains largely unclear. The canonical model used to explain transient LMXBs has historically been the Disk Instability Model (DIM; Osaki 1974; Lasota 2001), which was initially invoked to explain outbursts in cataclysmic variables and then extended to accreting NSs and BHs (see Hameury 2020, for a recent review of the DIM in LMXBs). According to such theory, outbursts are initiated from thermal-viscous instabilities starting as the cold disk in quiescence accumulates mass from the companion star. The increase in temperature and ionization caused by the instability will then propagate throughout the disk as a heating front, to the point where the cold quiescent disk transitions to a hot "outbursting" one and accretion onto the compact object is established. The heating front will, however, activate different parts of the disk at different times, causing a delay between the optical (originating from the outer disk) and the X-ray (from the inner disk and the Comptonizing hot flow) light curves of an outburst. However, optical-to-X-ray delays have been measured only for a handful of sources, mostly BH LMXBs (e.g. Orosz et al. 1997; Jain et al. 2001; Zurita et al. 2006; Bernardini et al. 2016; Tucker et al. 2018) and a few NSs, such as Aquila X-1 (Russell et al. 2019), SAX J1808.4-3658 (Goodwin et al. 2020) and MAXI J1807+132 (Rout et al. 2025b). In all these cases, the optical start of the outburst has been observed to precede the X-ray start by several days.

The chances to catch the onset of new LMXB outbursts in the X-rays have significantly increased with the launch of the *Einstein Probe* (EP, Yuan et al. 2025) mission. Thanks to the unprecedented "grasp" (field of view times sensitivity) of the Wide-field X-ray Telescope (WXT, Cheng et al. 2025), at least one order of

magnitude larger than current and past X-ray wide-field monitors, and in the soft X-ray range, EP is able to detect X-ray Galactic sources with a 0.5–10 keV luminosities of about 10^{35} erg/s (assuming an 8 kpc distance) or lower. In its 1.5 years of operations, EP has indeed been the first telescope to catch the onset of new outbursts from several known LMXBs (Xu et al. 2024; Wang et al. 2025; Sun et al. 2025), including the transient NS LMXB Aquila X-1 (Liu et al. 2024), hereafter Aql X-1. Aql X-1 (V1333 Aql) is one of the first NS LMXBs ever discovered, with its identification dating back to 1973 (Kunte et al. 1973). Thanks to its proximity, at a distance of 6 ± 2 kpc (Galloway et al. 2008; Mata Sánchez et al. 2017), and its frequent, almost yearly, outbursts (Šimon 2002; Niwano et al. 2023; Heinke et al. 2025), Aql X-1 has been studied in great detail over the last few decades, becoming one of the archetypal transient NS LMXBs. The donor star has been identified as a K-type star (Mata Sánchez et al. 2017) orbiting around the NS in a 18.95 hr orbit (Chevalier & Ilovaisky 1991). Type-I X-ray bursts have been frequently observed from the source (see, e.g., Mandal et al. 2025), providing a secure identification of the accreting compact object as a NS (Galloway et al. 2008) and of the NS spin frequency through the detection of burst oscillations (549 Hz, Zhang et al. 1998). The source is also classified as an intermittent accreting millisecond pulsar (Di Salvo & Sanna 2022), briefly displaying X-ray pulsations at comparable frequency but only over a brief 150-s time interval (Casella et al. 2008). During its outbursts, Aql X-1 displays a canonical hysteresis cycle, undergoing transitions through the main known LMXBs spectral states (Maitra & Bailyn 2004; Güver et al. 2022; Putha et al. 2024). In the last two years, the source underwent two outbursts, a bright one in 2024, discussed in this paper, and one significantly fainter in 2025 (Alabarta et al. 2025; Rout et al. 2025a). The 2024 bright outburst of the source was discovered by WXT onboard EP on September 14th, 2024 (Liu et al. 2024). The onset of the outburst was confirmed at optical wavelengths by XB-NEWS later that same day (Rout et al. 2024). Multi-band follow-ups were performed in the following weeks with the Very Large Array (Russell et al. 2024) and MeerKAT (Grollimund et al. 2024) in radio and with *Swift* (Mandal & Pal 2024) and SVOM/ECLAiRs (Le Stum et al. 2024) in X-rays. In this work, we analyse the 2024 outburst of Aql X-1 with *Einstein Probe*, *NICER*, *NuSTAR*, *Swift* and *Las Cumbres Observatory* data. In Section 2, we report on the data reduction procedure used for all the aforementioned observatories. A detailed description of the data analysis, including a multi-band analysis of the outburst light curves (Section 3.1), a broadband X-ray spectral analysis (Section 3.2) and an X-ray timing analysis (Section 3.3) is illustrated in Section 3. Finally, Section 4 is devoted to a discussion of the results presented in the previous sections, while conclusions and future prospects are presented in Section 5.

2. Observations & Data Reduction

The outburst studied in this work started in early September 2024, lasting until mid-November 2024. Throughout this period, Aql X-1 was the subject of a very dense monitoring campaign that provided almost daily coverage of the source for most of its active phase. In this paper we use data from several X-ray instruments as well as optical data, as mentioned above. In the following Sections, we illustrate the data reduction procedure employed for each instrument. As a thorough analysis of the Type-I X-ray bursts activity goes beyond the scope of this paper, we have systematically excluded all the bursts from the Good Time Intervals used for each dataset considered here. Details on all the

X-ray observations used in this work are reported in Table A.1. All X-ray data reduction processes have been carried out with HeaSOFT v. 6.33.1.

2.1. Einstein Probe

The 2024 outburst was first discovered by WXT onboard EP on September 14th, 2024 (Liu et al. 2024). The source location has been covered daily by the monitor over a six-month period starting in July 2024 and ending on October 10th 2024, when unfortunately the source became not visible, thus interrupting the WXT monitoring of the 2024 outburst. We have gathered all WXT data from September 8th, 6-days prior to the detected outburst onset, until the last day that the source was visible. The total exposure of the accumulated WXT data is about 0.4 Ms. In order to extract a WXT light curve, we ran the processing pipeline available within the WXT Data Analysis Software (WXTDAS) to produce cleaned event files for each observation. A circular, 9'-radius region centred on the source position was used to extract source photons. A region of the same size, but located away from the source, was used as the background region. We finally used `Xselect` to extract background-subtracted light curves from the cleaned event files in the 0.5–4 keV energy band.

After the discovery of the outburst, we triggered an X-ray campaign with the Follow-up X-ray Telescope (FXT) onboard EP, collecting 5 observations in total with an average 2-day cadence. The observations were performed with one detector (A) in Partial Window mode (PW), and the other (B) in Timing Mode (TM). However, the source quickly became too bright for the PW observations, causing severe pile up at fluxes higher than 40 mCrab. By visually inspecting the pattern distribution plots created with the `fxtplotgrade` task, we checked whether the pile-up effect could be effectively mitigated using annular regions with increasingly larger inner radii, without success. As such, in the following we only consider the data taken in TM, which is significantly less impacted by pile-up. Rectangular regions of 3' length and 1' width aligned with the window are used for both source and background extractions. Further processing of the data is performed with the FXT Data Analysis Software Package (FXTDAS v.1.20) and `Xselect`. As the count-rate was visibly increasing within obsID 06800000125 (MJD 60581.692), we broke down the observation into two segments and extracted science products separately.

2.2. NICER

NICER extensively monitored the 2024 outburst, with near-daily coverage totaling 44 observations. These data were processed using the `nicer12` pipeline and default screening settings. In particular: i) we excluded time intervals in the proximity of the South Atlantic Anomaly; we considered only data taken with ii) elevation angle of at least 30° over the Earth's limb; iii) minimum angle of 40° from the bright Earth limb; iv) maximum angular distance between the source direction and *NICER* pointing direction of 0.015°. We note that the use of HEASoft v6.33.1 substantially mitigated the impact of the optical leak reported in May 2023. We inspected each light curve to check for the presence of Type-I X-ray bursts or other flares of non-physical nature, such as overshoots caused by charged particle contamination¹. The intervals corresponding to these episodes were excluded from further analysis. Finally, some observations showed

significant variability from one orbit to another. In those cases, we extracted science products separately for each orbit. In particular, this was the case for obsIDs: 7050340108, 7050340109, 7050340110 and 7675010106, which were broken down in 3, 3, 3 and 2 segments, respectively. We produced the spectra and background files with the `nicer13-spect` pipeline, using the SCORPEON default model for the creation of the background file.

2.3. NuSTAR

NuSTAR observed Aql X-1 twice during the 2024 outburst, on September 23rd and October 19th, for a total exposure of 38.5 ks. We analysed the data using standard tools provided by the NuSTARDAS package (version v.2.1.4a). The source spectrum was extracted from a circular region with a 100'' radius centered on the source coordinates. To mitigate potential background non-uniformity across the detector, background spectra were obtained from four circular regions, each approximately 50'' in radius, positioned at various source-free locations within the field of view. Light curves were extracted using `Xselect` and visually inspected for the presence of Type-I X-ray bursts. To isolate the persistent emission, we used `NuPRODUCTS` to extract spectra and light curves from an event file in which any such bursts had been filtered out.

2.4. Swift

The Ultra-Violet/Optical Telescope (UVOT; Roming et al. 2005) on board *Swift* observed Aql X-1 multiple times during the early rise and peak of its 2024 outburst. UVOT provided coverage in all six filters (*v*, *b*, *u*, *uvw1*, *uvw2*, and *uvw2*), although not every filter was used in each observation. We reprocessed all data starting from the raw sky images and combined exposures from individual visits using the `uvotimsum` tool. Source magnitudes were extracted with `uvotsource`, adopting a circular extraction region with a 5'' radius centered on the source. The background level was estimated using a nearby 10'' radius circular region free of contaminating stars. Aperture corrections were applied using the default curve-of-growth method. For each observation, source magnitudes were measured in the Vega system, and statistical and systematic uncertainties were combined in quadrature. When the source was not significantly detected in a given filter, we report the corresponding 3 σ upper limits. A complete summary of the measurements is provided in Table A.2.

2.5. Las Cumbres Observatory

Aql X-1 is one of the sources regularly monitored with the Las Cumbres Observatory (LCO) 1-m and 2-m telescopes as part of the Faulkes Telescope Project² (Lewis et al. 2008). Observations were performed using the *V*, *R* Bessell filters and the SDSS *g'*, *r'*, *i'* and *z'* filters. The optical magnitudes were extracted after performing multi-aperture photometry (MAP; see Stetson 1990) using the “X-ray Binary New Early Warning System” (XB-NEWS) pipeline (Russell et al. 2019; Goodwin et al. 2020; Alabarta et al, in prep). XB-NEWS first detects sources in each image using SExtractor (Bertin & Arnouts 1996) and then gets the astrometric solution with astrometry.net (Lang et al. 2010), matching the detected sources to Gaia DR2 positions. If the target is not detected within 1'' of its known coordinates at the default threshold, the pipeline re-runs using a lower threshold or forced photometry is performed at the target position. Then,

¹ https://heasarc.gsfc.nasa.gov/docs/nicer/analysis_threads/overshoot-intro/

² <http://www.faulkes-telescope.com>

photometry is performed for all sources in the image using both MAP and fixed-aperture photometry, with apertures scaled to several multiples of the point-spread function full-width half-maximum (PSF FWHM). Light curves are constructed using the DBSCAN clustering algorithm (Ester et al. 1996). Calibration of the i' and g' magnitudes is performed with an enhanced version of the ATLAS-REFCAT2 catalogue (Tonry et al. 2018), which incorporates the Pan-STARRS DR1 (Chambers et al. 2016) and APASS DR10 (Henden et al. 2018) catalogues. A photometric model is fit to the light curves (in magnitudes) of matched and unmatched sources, including spatially variable zero-points, PSF-based terms, and source-specific mean magnitudes (Bramich & Freudling 2012). This process is done iteratively, mitigating the effects of intrinsic variability with outlier down-weighting. For SDSS i' and g' filters, XB-NEWS uses the Pan-STARRS1 standard i_{P1} and g_{P1} magnitudes in the AB system. The final model is applied to calibrate all the light curves, including those corresponding to the target. Finally, magnitudes with uncertainties > 0.25 mag are excluded from this study, as they are considered unreliable.

3. Data analysis

This section reports the procedure used to analyse the data and the main results. All the spectral results reported here have been obtained with `Xspec` (Arnaud et al. 1999) version 12.14.1. In all cases, where the interstellar absorption `TBABS` model is adopted, we consistently used photoelectric cross-sections and elemental abundances from Verner et al. (1996) and Wilms et al. (2000), respectively.

3.1. Multi-band light curves in the early rise phase

Figures 1 and 2 (top panel) show the EP/WXT light curve of the 2024 outburst of Aql X-1 in terms of X-ray luminosity and count rate, respectively. For the analysis of the EP/WXT data we systematically used an absorbed power-law model, i.e., `tbabs × powerlaw` in `Xspec`. Unfortunately, the poor statistics in each spectrum and the limited energy band, 0.5–4 keV, prevent us from using more sophisticated and physically reliable models. Subsequently, rather than attempting to extract physical parameters from this modeling, we use the spectral analysis solely to estimate the X-ray flux in the 0.5–10 keV range via the `cflux` component in `Xspec`. Finally, we calculate the X-ray luminosity in the above range by assuming a distance of 4.5 kpc (Galloway et al. 2008). In the plot, and for the rest of this manuscript, we mark the first detection of the source by EP, reported by Liu et al. (2024), as T_0 , where $T_0 = 60567.5$ MJD. According to our results, EP first detected Aql X-1 at an X-ray luminosity of about 10^{35} erg s $^{-1}$. The 4 data points prior to T_0 have been extracted by stacking all the WXT data taken after T_0 –6 d by means of the `XIMAGE` software (version 4.5.1), using the `sosta` command. We used time bins varying from 2 to 0.5 days, chosen in order to accumulate at least 10 ks total exposure for point. Such a stacking procedure allowed us to obtain marginally significant (signal-to-noise ratio between 2.5 and 3.0 σ) detections of the source during the 2 days before T_0 at a WXT count-rate (in the 0.5–4 keV band) of $(5.8 \pm 1.8) \times 10^{-3}$ cts/s. On the other hand, even after merging the data, we could not detect the source in the previous 2-day intervals and could only derive upper limits (at confidence levels of 3– σ) of 6.7×10^{-3} cts/s and 3.5×10^{-4} cts/s in the T_0 – 4 d and T_0 – 5 d intervals, respectively. In order to estimate the WXT count-rate corresponding to quiescence, we used the minimum

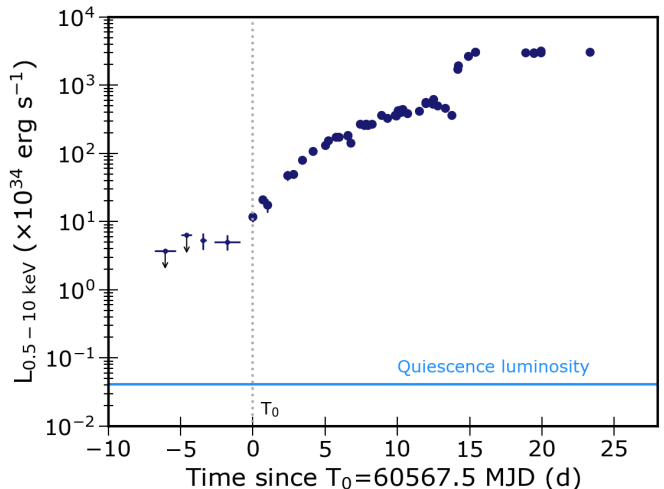


Fig. 1. EP/WXT light curve of the 2024 outburst of Aql X-1. The luminosity has been extrapolated to the 0.5–10 keV range (see text for more details). The quiescence level, measured by Cackett et al. (2011), is marked with a horizontal solid cyan line, while the vertical dotted gray line indicates T_0 , the time of the first bright (significance above 3– σ) detection by EP. The first two points correspond to non-detections and the corresponding upper limits are marked with vertical downwards arrows. The third and fourth points are instead marginal detections (significance between 2 and 3– σ) and are therefore represented with circular points but with smaller size compared to the remaining points.

flux measured with *Chandra* in quiescence as reported by Cackett et al. (2011), 3×10^{-13} erg cm $^{-2}$ s $^{-1}$ in the 0.5–10 keV energy range, and converted it into a WXT count-rate under the assumption of an absorbed power-law spectrum with fiducial Γ index of 2.0 and N_H of 5×10^{21} cm $^{-2}$ (see below). We thus estimate that the X-ray flux of Aql X-1 in quiescence would correspond to a WXT 0.5–4 keV count-rate of $\sim 4 \times 10^{-5}$ cts/s.

Besides EP, the rising phase of the Aql X-1 2024 outburst has been extensively covered by a variety of multi-band instruments. For the hard X-ray band, we collected the 2–20 keV light curve obtained by *MAXI* (Matsuoka et al. 2009) from its public repository³. The light curve is displayed in Fig. 2 Top panel with pink diamonds. For clarity, upper limits prior to the first *MAXI* detection are not shown in the figure. The optical-to-UV light curves in magnitudes are displayed for all the filters used in this work in the Middle (*Swift*/UVOT) and Bottom panels (LCO) of Fig. 2. The earliest UVOT observation on 2024 September 19 (MJD 60572.97) yielded only upper limits in the u , $uvw1$, $uvw2$, and $uvw3$ filters, while marginal detections were obtained in v (17.7 ± 0.2 mag) and b (18.7 ± 0.3 mag). In subsequent observations the source brightened in all filters, with the brightest measurements occurring around October 1–2 (MJD 60584–60585). The UV rise measured by UVOT showed a similar brightening to the optical light curve, confirming the rapid flux increase during the early outburst phase. The optical light curves are consistent with a steady rise in flux from the quiescence level, followed by a shallower rise after \sim MJD 60582.

3.1.1. Phenomenological analysis

In this section, we try to estimate the time at which the outburst started (T_{start}) at different wavebands. Such a task presents different challenges depending on the specific instrument used. Indeed, while the LCO data clearly show the transition from quie-

³ <http://maxi.riken.jp/top/lc.html>

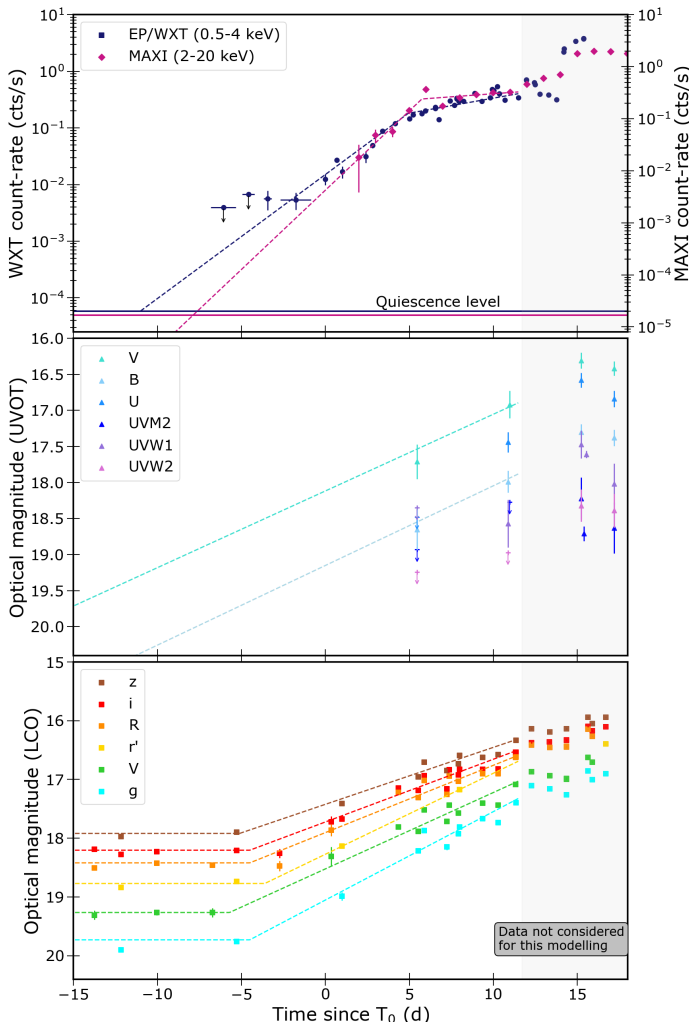


Fig. 2. Multi-band light curves of the outburst rise of Aql X-1, including: EP/WXT (blue) and MAXI (magenta) in the *Top* panel, *Swift*/UVOT in different filters in the *Middle* panel and LCO in the *Bottom* panel. The horizontal solid lines in the *Top* panels are set at the equivalent WXT and MAXI count-rates for the quiescent luminosity in Cackett et al. (2011). The phenomenological trends estimated for each data set are shown with superimposed dashed lines. Upper limits are marked with vertical downwards arrows.

escence to outburst roughly 5 d prior to T_0 , Aql X-1 was not detected in quiescence by either EP, MAXI or *Swift*/BAT. This lack of X-ray detection of the quiescent state makes it difficult to pinpoint the time of the X-ray rise, $T_{\text{start},X}$ at which the source rose from quiescence to outburst in X-rays. However, an attempt to obtain an indication of $T_{\text{start},X}$ can be done by extrapolating the rising trend in the EP and/or MAXI data down to the quiescence level. In order to do that, we used the `curve_fit` algorithm in `scipy` to obtain a phenomenological description of the rising phase in all the light curves used in this work. Depending on the different observed trends and completeness in coverage, we used different functions:

- The X-ray data, both EP and MAXI, show a general rising trend with a “knee” roughly 5 d after T_0 . We thereby used a broken exponential of the form:

$$f_X(t) = \begin{cases} A_X e^{\alpha_1 t}, & t \leq T_{\text{knee}}, \\ A_X e^{(\alpha_1 - \alpha_2)T_{\text{knee}}} e^{\alpha_2 t}, & t > T_{\text{knee}}. \end{cases}$$

where T_{knee} marks the time at which the index of the exponential switches from α_1 to α_2 and A_X consists in the normalization of the exponential.

- The LCO data in all filters are almost flat until about 5 d prior to T_0 and then start rising. We therefore used a piecewise linear fit to the magnitudes (an exponential rise in flux) of the form:

$$\text{mag}_{\text{opt}}(t) = \begin{cases} \text{mag}_Q, & t \leq T_{\text{start, opt}}, \\ \text{mag}_{0,\text{opt}}(t - T_{\text{start, opt}}) + \text{mag}_Q, & t > T_{\text{start, opt}}. \end{cases}$$

where mag_Q is the observed magnitude in quiescence and $T_{\text{start, opt}}$ is the time at which the source transitions out of quiescence in this waveband.

- The UVOT data are characterised by a significantly sparser coverage, preventing us from obtaining a comparably detailed description of the rise. We therefore used a simple linear function (exponential rise in flux) of the form: $\text{mag}_{\text{UV}} = A_{\text{UV}} t + b$.

We report the results of this phenomenological analysis in Table A.2. According to such parameterization, in X-rays the rise proceeded in two steps: a steeper rise until $T_{\text{knee}} \sim T_0 + 4.7$ d with index $\alpha_1 = 0.5$ and a slower one beyond T_{knee} characterised by $\alpha_2 \sim 0.15$. The intersection between the EP quiescence level and the steeper exponential was estimated to be $T_0 - 11.7$ d, which can be regarded as a lower limit on $T_{\text{start},X}$, assuming the rise followed the same functional form. We performed the same analysis using the MAXI data and obtained similar values for T_{knee} , α_1 , α_2 and $T_{\text{start},X}$, of ~ 5.6 d, 0.7, 0.17 and $T_0 > -6.5$ respectively.

For the optical analysis, we fixed the quiescent magnitude level, mag_Q , to the values obtained from the analysis of the entire LCO data repository of Aql X-1 in quiescence (Alabarta et al., in prep.) to reduce the number of degrees of freedom and ease the fit. The resulting values for $T_{\text{start, opt}}$ vary from $T_0 - 5.5$ d (filter z') to $T_0 - 3.6$ d (filter r'). The slope of the lines shows a clear trend depending on the filter, with an increase in a_{opt} with decreasing wavelength, going from $a_{\text{opt}} \sim -0.09$ with the z' (IR) filter to $a_{\text{opt}} \sim -0.14$ with the g (blue) filter. Finally, we applied this phenomenological approach only to the data taken with filters B and U of UVOT, as the light curves in the other filters had too few data points. The slope a_{UV} in filter U , ~ -0.15 , is interestingly similar but slightly larger than the one obtained for a_{opt} in the blue filter. Along with the phenomenological analysis described in this Section, we used an alternative method to characterize the temporal evolution of the multiwavelength emission from Aql X-1 during the early stages of its 2024 outburst within a non-parametric framework by performing Gaussian Process regression on the light curves (for a review, see Aigrain & Foreman-Mackey 2023). By applying this technique, we confirm a start of the X-ray outburst after $T_0 - 10$ d. More details about the employed methodology are provided in the Appendix, Section B.

3.2. Spectral analysis

All the spectra used in this work were rebinned with FTGROUP-PHA following the Kaastra & Bleeker optimal binning algorithm (Kaastra & Bleeker 2016) in order to have at least 25 counts per bin. In all the spectral analyses performed here, we fixed the equivalent hydrogen column density N_H to the value of 0.5×10^{22} cm $^{-2}$ (see also Putha et al. 2024). This choice was motivated by the fact that N_H was consistently found to be close to this value in the individual fits, and fixing it mitigated degeneracies with other spectral parameters. When fitting together data

from multiple instruments, a multiplicative constant component was added to account for cross-calibration uncertainties, and we verified that differences in the constant values between instruments remained within 20%. We kept data in the following energy ranges: for *NICER* we only included data between 0.7 and 10 keV, as the background became dominant outside this range; for *NuSTAR* we considered the entire 3-79 keV range for ObsID 91001338002, while we ignored all data above 30 keV in the other *NuSTAR* observation, ObsID 91001345002, where the emission was significantly softer; for EP/FXT we ignored all data below 1 and above 9 keV and systematically ignored the 2-2.5 keV region due to known calibration issues for spectra taken in TM mode (EP Science Center, private communication). Because of those calibration issues, we also included a 1% systematic error in the analysis of FXT data.

In order to maximise the statistics and improve the quality of our spectra, we have fitted together spectra which were taken close in time and had similar spectral shape and X-ray flux. In the following, we will dub these groups of spectra “Epochs”. Dates and corresponding spectra for each Epoch are presented in Table A.1. In Fig. 3 we display the light curve and the HID produced with all the *NICER* observations used in this work. In the light curve we marked down the dates of the observations with *NuSTAR* and EP/FXT. As evident from the HID, where selected points are labeled with their assigned Epoch, the outburst displayed the typical q-shaped track with a clear diagonal hard-to-soft transition from Epoch 6 on. Our strategy in performing the spectral analysis was to start from the two Epochs with coverage from *NuSTAR* and *NICER*, Epochs 3 and 28, where the broadband spectral coverage provides reliable physical modelling. The spectral shapes are significantly different across the Epochs, as expected considering their distinct location in the HID, with Epoch 3 having a cut-off power-law shape extending down to the end of the nominal energy range of *NuSTAR* and Epoch 28 being characterized instead by a seemingly thermal profile ending at about 30 keV. For both Epochs, we used a blackbody component `bbodyrad` convolved with `thcomp` (Zdziarski et al. 2020), to consider both the Comptonization spectrum and the thermal spectrum which provides the seed photons. As an extra-component in the soft X-rays was present, we included a `diskbb` component, as well. The statistical need for this extra component was tested by comparing the fit with and without the additional disk contribution and then running `ftest`. We obtained negligible probabilities of improvement by chance for both Epochs, of $\sim 10^{-61}$ and $\sim 10^{-38}$, strongly confirming that an additional thermal component is required by the fit. When modelled with these continuum models, both spectra show clear residuals between 6-7 keV, indicating the presence of reflection. We therefore included different flavors of the `relxill` (García et al. 2013, and references therein) model to take into account reflection in different spectral states. In particular, the self-consistent `relxill1Cp` model (García et al. 2014), which describes reflection of a Comptonized continuum off the accretion disk, was used for Epoch 3. However, as `relxill1Cp` assumes a seed photon temperature of 0.05 keV, which is unrealistically low for the NS LMXB case, we also multiply that component by `expabs`, a component able to mimic the low-energy roll-over expected for a higher seed photons temperature. Epoch 28 was too soft to be properly modelled with `relxill1Cp`, leading us to use `relxill1NS` instead (García et al. 2022), where the continuum incident on the disk is a blackbody. The two models used, labelled “H” (hard) and “S” (soft) for Epochs 3 and 28, respectively, are the following:

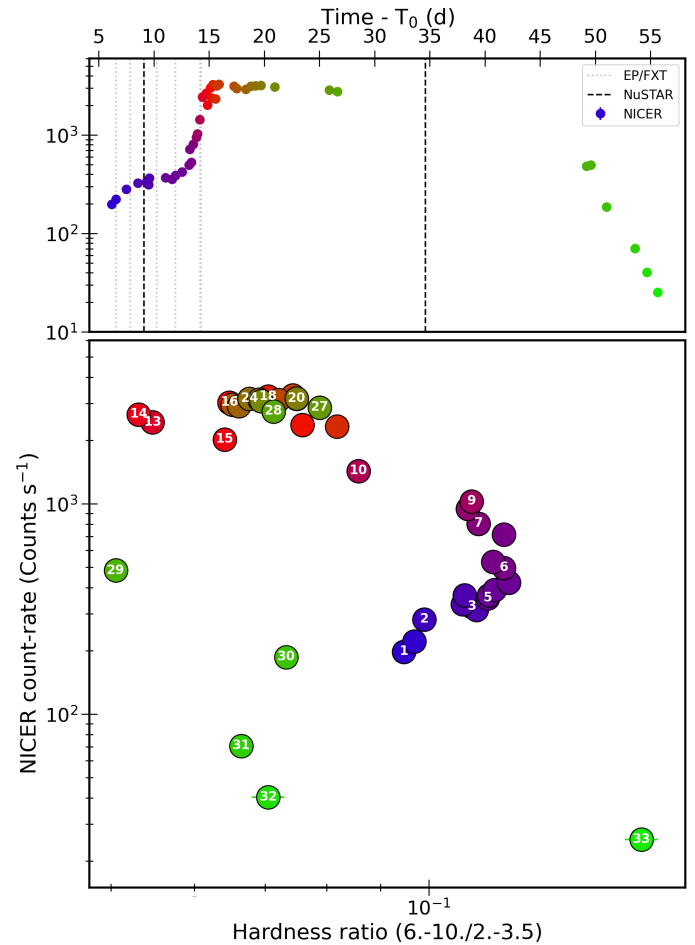


Fig. 3. *NICER* light curve (Top) and HID (bottom). The total count rate has been extracted in the 1-10 keV band. The hardness is defined as the ratio between the hard band (6-10 keV) and the soft band (2-3.5 keV) count rates. A color map going from blue to red and to green is used to indicate the time evolution. The vertical lines in the top panel mark the times of the *NuSTAR* (dashed) and EP/FXT (dotted) observations. The labels on top of selected circular data points in the bottom panel indicate the corresponding Epoch.

$$\text{Model H: } \text{tbabs} \times (\text{thComp} \times \text{bbodyrad} + \text{diskbb} + \text{expabs} \times \text{relxill1Cp}) \quad (1)$$

$$\text{Model S: } \text{tbabs} \times (\text{thComp} \times \text{bbodyrad} + \text{diskbb} + \text{relxill1NS}) \quad (2)$$

An overview of all the parameters included in the models and their best-fit values are reported in Table A.3. In Model “H”, for physical consistency, we tied $E_{\text{cut-off,low}}$ to $3 \times kT_{\text{bb}}$, we bound together the photon indices Γ and electron temperatures kT_{e} of `thcomp` and `relxill1cp` and fixed the reflection fraction parameter f_{refl} to -1 so that we only consider the reflection spectral component. Some parameters were not well constrained by the fit, so that we froze them to typically adopted values for LMXBs (e.g. Saavedra et al. 2023; Ludlam 2024; La Monaca et al. 2025): the emissivity index ϵ was set to 3, the Fe abundance A_{Fe} to 1 and the density parameter $\log N$ to 19. We show the broadband spectra for Epochs 3 and 28, along with the best-fit models used to describe them, in Fig. 4.

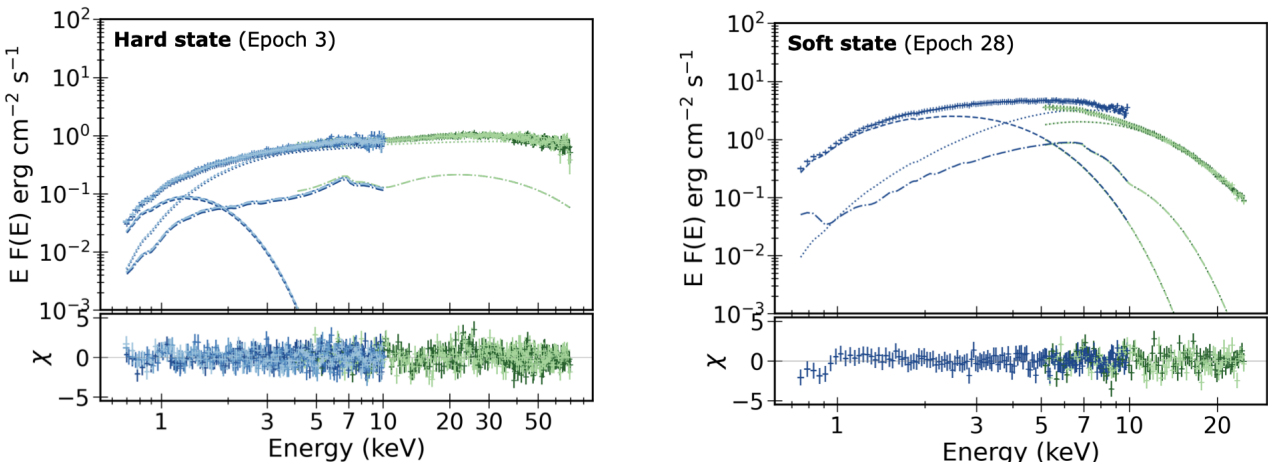


Fig. 4. Broadband *NICER* (different shades of blue to distinguish between the *NICER* spectra used in the same Epoch) and *NuSTAR* (different shades of green to distinguish FPMA and FPMB) spectra for Epoch 3 (left, fitted with Model H) and Epoch 28 (right, fitted with Model S) and residuals. Different line styles were adopted to distinguish between the different components: dash for `diskbb`, dot for `thcomp×bbodyrad` and dash-dot for `relxillCp` (left panel) and `relxillNS` (right panel).

For the remaining Epochs, with the exception of Epochs 30–34 (see below), we have adopted Model “H” or Model “S”, but under some assumptions, as the lack of data above 10 keV limits significantly the quality of our fits. First of all, we fixed kT_e in `thcomp` to 23.0 keV (3.5 keV) for the spectra modelled with Model “H” (“S”), i.e. to the value obtained for Epoch 3 (28), which was taken in a similar state. While realistically we expect kT_e to change throughout the outburst, we consider these assumptions acceptable as: i) for spectra described with “H”, where kT_e is above 10 keV, any impact that variations of kT_e may have on data with only soft X-ray coverage would be negligible; ii) for spectra described with “S”, the limited statistics does not allow to constrain kT_e , so that the fit is mostly insensitive to variations of this parameter. Additionally, for similar reasons, we froze all the parameters of the reflection component, being it `relxillCp` or `relxillNS`, with the exception of the normalisation K_{refl} . While this general strategy allows us to obtain acceptable fits for each Epoch, we of course will not consider this as a proof that the reflection parameters, as well as kT_e , do not change from one Epoch to the other. Finally, a different strategy has been adopted for the last four Epochs, corresponding to the decay phase of the outburst. Given the much lower count-rate compared to the rest of the outburst, we had to first remove the reflection component (Epochs 29–31) and then also the disk component (Epochs 32–33), as they were no longer required by the fit.

The results of our individual fits are presented in Table A.4 and in the tower plot in Fig. 5. From the normalization values of the `bbodyrad` (K_{bb}) we extracted the radius of the blackbody emitting region R_{bb} (in km) using the formula: $K_{\text{bb}} = (R_{\text{bb}}/D_{10})^2$, where D_{10} is the source distance in units of 10 kpc, set in this case to 0.45 kpc (as reported by Galloway et al. 2008). Similarly, we estimated the disk inner radius from the normalization of `diskbb` (K_{disk}) using the formula: $K_{\text{disk}} = (\xi f_{\text{color}}^2)^{-2} (R_{\text{disk}}/D_{10})^2 \cos i$, where ξ is the Kubota et al. (1998) correction factor equal to roughly 0.4, f_{color} is the color correction factor equal to 1.7 (Shimura & Takahara 1995) and i is the system inclination, fixed to 30° according to the results of this and previous papers (e.g. Ludlam et al. 2016). We note that the correction factor ξ accounts for the torque-free condition, which might not be always valid for NS systems, so that our estimates for R_{disk} are probably systematically underestimated and should

not be taken at face value. As evident from the tower plot, the outburst can be broken down in 4 phases (highlighted with different colors in the plot): a relatively “slow” rise lasting for a week (Phase “1”), a dramatically rapid, a few days-long, flux increase (“2a”, “2b”), a several weeks-long plateau at the outburst peak (“3”) and finally a decay to quiescence (“4”). The highly dynamic spectral variability in the second phase can also be inferred by the fact that all the Epochs from 6 to 20 have been taken between September 27th to September 30th. In order to zoom-in on this particularly eventful phase of the outburst, we show a 3-days light curve of this time period, along with the different energy spectra, power density spectra (see Section 3.3) and hardness ratio in Fig. 6. The plot clearly shows that in about half a day the count-rate more than doubles, the hardness ratio drops by a factor of 3, and the shapes of both the energy and power density spectra change abruptly and dramatically.

3.3. Timing analysis

For the timing analysis, we corrected the photon arrival times of the source event files to the Solar System barycentre using the `barycorr` tool, the most recent calibration files, and the DE405 ephemeris. We adopted the known coordinates of the source, R.A. = 19^h11^m16^s05713, Decl. = +00°35'05.8682 (J2000.0) (Gaia Collaboration 2020). We considered all the X-ray observations used in this work, selecting as energy ranges: 0.3–12 keV for *NICER* and EP and 3–79 keV for *NuSTAR*. Single observations split into “Epochs” for the spectral analysis were here analysed together. We extracted the power density spectrum (PDS) by averaging over 64-s long segments with time bins of 1.0 ms. In order to correct for the dead-time, we applied the *NuSTAR* PDS using the Fourier Amplitude Difference (FAD) method (Bachetti & Huppenkothen 2018) as implemented in *Stingray* (Huppenkothen et al. 2019; Bachetti et al. 2024). For each PDS, we estimated the fractional rms over the entire frequency band by modelling the PDS in *XSPEC* with a combination of Lorentzian functions and a constant to account for the Poisson noise contribution. We show the temporal evolution of the rms for the 0.3–12 keV *NICER* PDS in the bottom panel of Figure 5. In order to estimate the “break” frequency ν_{break} dividing the band-limited noise dominated part of the PDS from the red noise (Wijnands & van der Klis 1999), we also analysed each PDS with a sin-

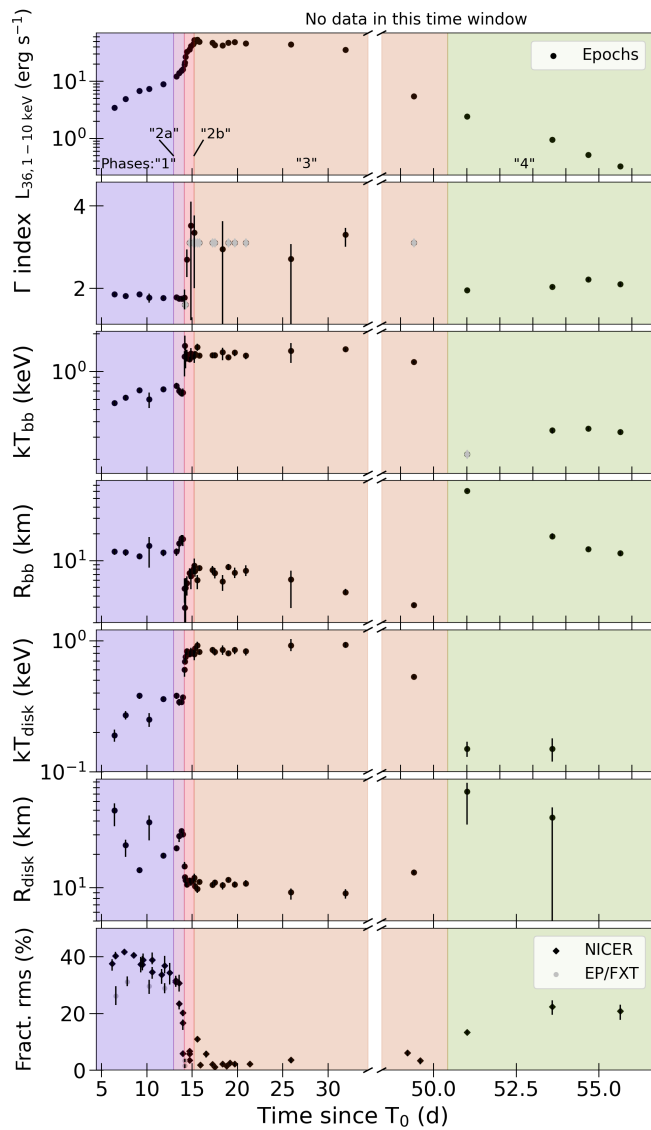


Fig. 5. Evolution of the main spectral-timing parameters of Aql X-1 during the 2024 outburst. In the top six panels (Luminosity in the 1 - 10 keV abnd, Γ index of the comptonizing medium, temperature and radius of the black body component, temperature and radius of the disk component), each point corresponds to a different Epoch. In the bottom panel (fractional rms), we distinguish instead between values obtained for *NICER* (black diamonds) and EP/FXT (gray circles). The fractional rms has been calculated considering the 0.01-1000 Hz frequency range and the 1-10 keV energy range. Parameters that were kept frozen during the fit are reported as gray diamonds.

gle Lorentzian with centroid fixed at 0 and used the estimated width as a proxy for ν_{break} (see Fig. A.1). We systematically inspected all PDS searching for QPOs and/or other discrete features over the 0.01-1000 Hz frequency range. In order to do that, we searched whether our fit with a sum of broad Lorentzians left any fine structures unmodelled in the residuals and modelled such features with an extra Lorentzian. We then considered significant all the features for which the ratio between the Lorentzian normalization and its $1-\sigma$ error was found higher than 3, corresponding to a statistical significance of $3-\sigma$. No significant discrete component was found from this search.

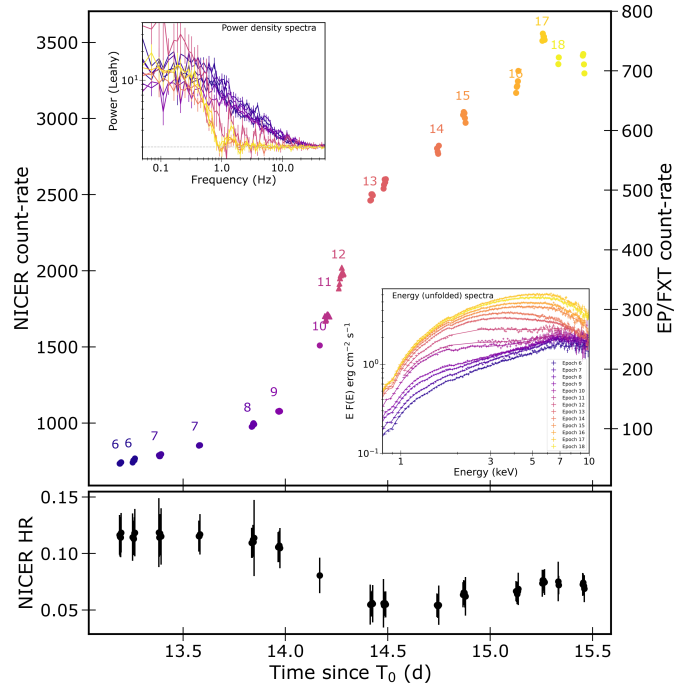


Fig. 6. *NICER* and EP/FXT light curves (Top) and hardness ratio (Bottom) during the spectral state transition period occurred between MJD 60580 and 60583. In the top panel, circles are used for the *NICER* observations and triangles for the EP observations. A time-bin of 240 s has been used for each observation. The Epoch in which each observation has been classified is indicated with superimposed labels. The inset plots show the evolution of the power density (top-left inset) and energy (bottom-right) spectra for the period considered.

4. Discussion

4.1. The “dawn” of the outburst

The early phases of LMXB outbursts represent, to date, a significantly underexplored regime of the activity from these sources. In this work, we have presented a multi-band monitoring campaign of the first \sim two weeks of the Aql X-1 2024 outburst from optical (LCO) to UV (UVOT) up to soft (EP/WXT) and hard (*MAXI*) X-rays. Using both a phenomenological approach and Gaussian Processes, we have estimated that: i) the optical outburst started around MJD 60562, \sim 5.5 d prior to the first EP detection, T_0 (Liu et al. 2024); ii) assuming that an exponential rise in X-ray flux observed by EP in the first days of monitoring can be extended down to the quiescent level, we can propose a lower limit on the beginning of the X-ray outburst to MJD 60556, \sim 11 d prior to T_0 ; iii) Aql X-1 was detected by EP in the two days prior to T_0 (albeit with a low SNR of 2.5-3), on MJD 60565, suggesting that the source was already active at that stage. These clues suggest two possible scenarios: firstly, that the X-ray outburst started earlier than the optical rise. However, we deem this unlikely because at the beginning of the X-ray outburst the emission is expected to be dominated by the hot flow / corona which Compton up-scatters photons from the disk once it heats up. The emission of X-ray photons, therefore, has to follow the formation of the heating front propagating throughout the disk, which is instead tracked by the optical rise. In the other, more likely scenario the optical rise preceded the X-ray. In that case, the X-ray rise date must be placed after the optical onset and before the first weak EP detection, i.e., between 60562-60565 MJD. Therefore, we propose an X-ray-to-optical

delay of $\lesssim 3$ days. This result is fully compatible with the 3-d X-ray-to-optical delay estimated for the Aql X-1 1997 outburst by [Shahbaz et al. \(1998\)](#). Interestingly, the delay is also similar to that measured for SAX J1808.4-3658 (4 d, [Goodwin et al. 2020](#)), but it is smaller than that obtained for MAXI J1807+132 (4–12 d, [Rout et al. 2025b](#)), which are to date the only other NS LMXBs for which X-ray-to-optical delays have been reported. This scenario also implies that the very early X-ray rise from quiescence to X-ray levels of $\sim 10^{35}$ erg s $^{-1}$ occurs much faster than during the portion we observed with EP. In this context, the initial fast X-ray rise may be connected to the evidence that the slope of the optical rises increases with frequency (see Figs. 2–B.1). In the optical regime, this phenomenon can be interpreted as a consequence of the outer disk heating as it brightens. As the temperature increases, the emission becomes bluer, resulting in the emission in the blue bands rising more rapidly than that in the red bands (e.g. [Maitra & Bailyn 2004](#); [Bernardini et al. 2016](#); [Koljonen et al. 2016](#); [Rout et al. 2025b](#)). Furthermore, we speculate that the (presumed) very fast initial rise might indicate the end of a propeller regime once the inflowing disk approaches the NS's magnetosphere, the accretion rate becomes high enough to overcome its magnetospheric pressure and the luminosity reaches about 5×10^{34} erg s $^{-1}$. A propeller phase has previously been invoked to explain the presence of a “knee” at a much higher X-ray luminosity level, i.e., at $\sim 5\text{--}6 \times 10^{36}$ erg s $^{-1}$, during the decay of two different Aql X-1 light curves, namely those of the 1997 ([Campana et al. 1998](#)) and 2010 ([Campana et al. 2014](#)) outbursts. It is also noteworthy that even the portion of the rise observed by both EP and MAXI shows a similar “knee”, occurring at about $T_0 + 5$ days and at a comparable luminosity ($\sim 2 \times 10^{36}$ erg s $^{-1}$), although in our case a similar explanation to the aforementioned papers can not hold, as the propeller effect would be weaker at higher luminosity. While the competition between the ram pressure of the accretion flow and the centrifugal barrier produced by the rotating magnetic field may plausibly account for this apparent “three-step” rise (initially very fast at $T < T_0$, fast between T_0 and T_{knee} , slow after T_{knee}), we note that, given the absence of detectable X-ray pulsations in our data, any role of the NS magnetosphere in this outburst of Aql X-1 should be regarded with caution.

4.2. The hard state (Phase “1”)

Our detailed spectral and timing monitoring of the source started 6 days after the first EP detection of the source and it consisted of 33 “Epochs” throughout the entire outburst. All spectra from Epoch 1 to 31 were analyzed with a model consisting of a disk blackbody emission, a Comptonisation spectrum and a reflection component (models “H” and “S”). For the second component, two different models were applied depending on the spectral shape of the incident spectrum: during Epochs 1–9 and 30–31, a Comptonization model (`relxillCp`) was used, whereas for Epochs 10–29, the incident spectrum was assumed to be a blackbody (`relxillNS`). According to the results of our spectral analysis and the main physical parameters trends displayed in Figures 5 and A.1, we can reconstruct the evolution of Aql X-1 during its 2024 outburst in five phases: “1”, “2a”, “2b”, “3” and “4”. Phase “1” lasted for about 7 days and entails Epochs from 1 to 5. Throughout this phase, the source shows a hard spectral shape, with a photon index Γ of ~ 1.8 . The blackbody temperature and radius are well constrained at around ~ 0.7 keV and $\sim 10\text{--}12$ km, respectively. The size of the blackbody component suggests that it arises from about the entire NS surface. On the other hand, the disk is significantly colder than the black body component,

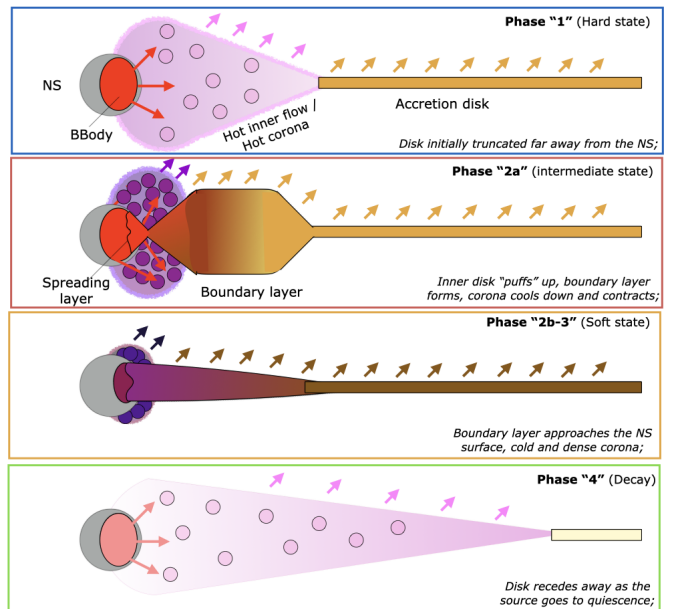


Fig. 7. Toy model of our proposed evolutionary scenario for the 2024 outburst of Aql X-1. The intensity of the color is qualitatively proportional to the temperature of each region; in particular the temperature increases from purple to pink for the hot inner flow, from yellow to brown for the disk and from salmon to dark red for the NS surface emission. The number of circular points inside the hot flow sketch represent its density.

but it gradually heats up throughout this phase, going from an initial temperature of 0.17 keV to 0.36 keV at the end of this phase. At the same time, the inner radius of the disk, estimated from the normalisation of `diskbb`, shows an initial decreasing trend from about 100 km to about 20 km, and then increases again, starting a puzzling trend that will be discussed further in the next section. The temperature of the electron corona kT_e can only be constrained during Epoch 3, the only one in this phase with *NuSTAR* coverage, giving a value of ~ 22 keV, a standard value for atolls in such a state (e.g. [Burke et al. 2017](#); [Di Salvo et al. 2019](#); [Anitro et al. 2021](#); [Marino et al. 2022](#); [Banerjee & Homan 2024](#); [Illiano et al. 2024](#)). The analysis of the reflection component for the same epoch provided a measurement of the system inclination, in the range $25^\circ\text{--}33^\circ$, compatible with what found by [Ludlam et al. \(2016\)](#) for the same source, and further confirming Aql X-1 as a moderately low-inclination LMXB. The inner disk radius can be constrained from the analysis of the reflection component in Epoch 3, where an upper limit of 10 gravitational radii R_G , about 20 km for a $1.4 M_\odot$ NS, was obtained, which is consistent with the disk radius measured from the `diskbb` normalization. Throughout this stage the fractional rms was relatively high but showed a general decreasing trend, going from 40% to about 30%. On the other hand, the value of the PDS break frequency ν_{break} showed a consistently increasing trend, which is considered as a signature of the accretion disk approaching the compact object (e.g. [Churazov et al. 2001](#)). The spectral and timing parameters are consistent with the accretion disk being truncated away from the NS and a rather hot inner flow or corona Compton-upscattering photons from the NS surface (as we sketch in the top panel of Fig. 7), a scenario consistent with a canonical hard state.

4.3. From hard to intermediate: witnessing the emergence of spreading and boundary layers? (Phase “2a”)

We classified in Phase “2” all the Epochs from 6 to 16. Despite the number of epochs being greater in number than the previous phase, the entire Phase “2” is remarkably shorter, lasting about 2 days. During this short time window, the source displays a dramatic evolution, which we break down here in two different sub-phases (“2a”, “2b”). Initially, while Γ remains at the same value of Phase “1”, the fractional rms starts to drop significantly from $\sim 30\%$ to $\sim 20\%$ and the luminosity starts to increase significantly, going from $\sim 7.2 \times 10^{36}$ erg s $^{-1}$ to 1.2×10^{37} erg s $^{-1}$ in about one day. The increase in luminosity is driven by an increase in the normalization, and therefore the size of the emitting region, of both the blackbody component and the disk component. The most trivial way to interpret the trend in the disk component would be to invoke a receding of the disk away from the compact object. However, if the disk was actually moving away, we would expect both its temperature kT_{disk} and the PDS break frequency ν_{break} to decrease; either trend is visibly absent from our results (see Fig. 5 and A.1). Additionally, the scenario of a disk receding during the state transition would also be at odds with the canonical truncated disk model (e.g. Done et al. 2007) and with what is typically observed in NS LMXBs going through a state transition (e.g. Marino et al. 2019; Rout et al. 2025c). According to the truncated disk model, the inner part of the disk in LMXBs in the hard state forms a vertically extended inner hot flow (e.g. Narayan & Yi 1995; Done et al. 2007; Poutanen & Veledina 2014), while, as the mass accretion rate and luminosity increase, the disk moves towards the compact object. By when the source reaches the soft state the disk should be a thin disk (Shakura & Sunyaev 1973) with no inner hot flow. When exactly the transition happens is still under debate (see e.g. discussions in Poutanen et al. 2018; Zdziarski et al. 2021a,b). In the case of NSs, the accretion flow needs also to slow down from the quasi-keplerian azimuthal velocity profile of the disk to match the spin of the star (this transition can take the form of a BL/spreading layer, depending on the mass accretion rate; e.g. Popham & Sunyaev 2001; Suleimanov & Poutanen 2006; Done et al. 2007; Inogamov & Sunyaev 1999, 2010). In order to resolve the tension between our data and the above model, we discuss two possible scenarios where an increase in disk normalization can be compatible with a constant (or even decreasing) inner disk radius. An increase in the disk normalization, which is a rough measure of the number of photons emitted by the region, could be explained with a sudden geometrical thickening, or a “puffing up”, of the disk as it pushes inside to approach the NS surface. Indeed, at sufficiently high accretion rates, part of the energy might be removed by advection instead of being radiated away. We have mimicked this scenario by replacing `diskbb` with `diskpbb` (Mineshige et al. 1994; Kubota et al. 2005), taking into account that turning up advection causes a deviation in the radial dependency of the disk temperature, $T \propto R^{-p}$, from a Shakura & Sunyaev (1973) thin disk. This model is routinely used for Ultraluminous X-ray sources (e.g. Bachetti et al. 2013; Pintore et al. 2025) and while the Aql X-1 accretion rate is by no means comparable to those sources, we still suggest that the structural modifications experienced by the accretion flow during the transition observed in Phase “2a” may be analogous. We show in Appendix C that using `diskpbb` both the increases in the inner radius of the disk R_{disk} and in size of the black body component R_{bb} can be replaced by a slight decrease of p , going from ~ 0.75 (as expected for Shakura & Sunyaev thin disks) to about 0.55. The scenario of an optically-thick disk

“puffed-up” by advection may suggest that during Phase “2a” we are witnessing the emergence of the puffed up inner disk and BL, which is expected to be more advection-dominated with respect to a Shakura & Sunyaev (1973) disk (see, e.g. Popham & Sunyaev 2001). The emergence of this BL might also be aided by the contraction of the corona, which in Phase “2a” is likely traced by the drop in the fractional rms. We sketch our proposed scenario in panel (b) of Fig. 7. An alternative possibility is that the trend in K_{disk} may be driven by changes in the correction factors f_{color} and/or ξ , which have been assumed constant throughout the outburst. For instance, f_{color} may have been higher in the hard state, as discussed by Ren et al. (2022, and ref. therein) for a different LMXB, and reached its canonical value of 1.7 only during the state transition.

4.4. A 12-h state transition? (Phase “2b”)

Going from Epoch 9 to Epoch 10, the spectral shape of the source (see inset in the low-right corner of Fig. 6) changed dramatically within about 12 hours. The evolution observed between these epochs is arguably one of the best documented spectral transitions in an LMXB to date, with almost hourly coverage thanks to the combined observations of *NICER* and EP. Because of the transition, we changed the best-fit model from model “H” to model “S” going from Epoch 9 to Epoch 10, meaning that the spectral shape of the spectrum illuminating the reflecting disk changed from a cut-off power-law shape to a blackbody. Γ , kT_{bb} and kT_{disk} all rapidly increase to values of about ~ 3 , ~ 1.4 keV and ~ 0.7 keV. An even more dramatic change can be observed for the physical sizes of both the black body component and the disk; as the latter suddenly approaches the NS surface, with the (apparent) inner radius moving from ~ 40 to ~ 15 km within a few hours, the size of the black body shrinks by a factor 4, to a size of 3–4 km, possibly now confined to a hot spot on the NS surface. The fractional rms continues its rapid decrease, dropping to a level of only 3–6% along the transition. While we cannot constrain the electron temperature in this phase, the rms evolution and the overall spectral softening strongly suggest that the corona may have experienced significant cooling during this epoch. We also note that as the corona becomes cold and dense, it will cover a smaller fraction of the NS surface (see Fig. 7, c), explaining the sudden shrinking of the hot spot size R_{bb} in Phase “2b”. Interestingly, such a trend during state transitions has been also invoked by Cavecchi et al. (2025) in a different context, where it was used to explain why Type-I X-ray bursts have different recurrence times trends between NS LMXBs spectral states. The ensemble of these spectral and timing clues clearly indicates that Phase 2 coincides with a remarkably rapid epoch of hard-to-soft transition and it can be identified as the intermediate state of Aql X-1. The notion that Aql X-1 experiences rapid, of the order of days, state transitions has been suggested before; Muñoz-Darias et al. (2014) report in their global study of hysteresis loops in NS LMXBs a hard-to-soft time scale of 1–4 days for Aql X-1, a result which can be also confirmed by visually inspecting light curves and/or hardness intensity diagrams of previous outbursts from the source (e.g. Tudose et al. 2009; Díaz Trigo et al. 2018) and by the recent broadband study of the 2023 outburst of the source by Yan et al. (2025). In the 2012 outburst of the transient NS LMXB 1RXS J180408.4-365028, a short-lived intermediate state was also identified and a hard-to-soft transition time-scale of 1 d suggested (Marino et al. 2019). Our results, however, allow for the first time to precisely identify the timescale of the full transition and to have unprecedented insights on the physical mechanisms

underlying spectral transitions in NS LMXBs. A causal connection between the formation of the boundary/spreading layers, the cooling/disruption of the corona and thereby the state transition could explain such a rapid state transition in Aql X-1. Beyond this single source, we propose that similar mechanisms may be at play in all state transitions in NS LMXBs. Indeed, while NS LMXBs typically perform state transitions in only a few days (see references above), LMXBs with BHs are often characterised by much longer hard-to-soft transitions, of dozens to hundreds of days (Tetarenko et al. 2016, but see Böck et al. 2011 for a reported very rapid state transition in the BH X-ray binary Cyg X-1). As BLs do not form in accreting BHs, in those systems the only source of soft photons responsible for coronal cooling is the disk, making the time to complete the transition significantly longer than in NS systems.

4.5. The soft state (Phase “3”)

After the spectral turmoil in Phase “2”, Phase “3” consists in a much longer and stable phase for the source. All spectra in this phase show consistent values in Γ (~ 3.0), kT_{bb} (~ 1.3 keV), kT_{disk} (~ 1.0 keV), R_{bb} (~ 8 km), R_{disk} (~ 15 km) and fractional rms well below 10%. Thanks to the broadband spectral analysis of Epoch 28, we can constrain the value of kT_e in this phase to ~ 3.3 keV. In this Epoch, the values of the inner disk radius provided by both `diskbb` and the reflection component `relxillNS` are well-constrained but only marginally consistent with each other, as the reflection component points to a slightly larger disk. We stress, however, that our estimates for R_{disk} are likely underestimated and, while the observed trends in these parameters are reliable, they should not be taken as real values. The R_{in} found by `relxillNS` is also compatible with the values obtained by the broadband spectral analysis of Aql X-1 for two previous outbursts (Ludlam et al. 2017). The inner radius is not the only physical parameter that seems to be the same between the broadband spectra in Epochs 3 and 28. The disk ionization $\log \xi$ and the reflection normalization K_{refl} seem to be broadly consistent as well between the Epochs, suggesting that the spectral evolution from one state to the other only marginally affects the reflection parameters and therefore the reflecting medium. It is noteworthy that while all the values above are also consistent with the parameters achieved at the end of Phase “2”, the size of the blackbody radius shows an increase with respect to the previous Phase. A plausible interpretation of this trend is that as it is being fed by the accreted material, the size of the spreading layer increases throughout this phase, heating up a gradually larger fraction of the NS surface with respect to Phase “1” (Inogamov & Sunyaev 1999, 2010; Suleimanov & Poutanen 2006). We conclude that throughout Phase “3”, the source lingered in a long and almost uneventful soft state.

4.6. The “dusk” of the outburst (Phase “4”)

In the final phase, which encompasses Epochs 30 to 33, the X-ray luminosity falls down below 10^{36} erg s $^{-1}$ as the source decays towards quiescence. The spectrum hardens significantly, with Γ , kT_{bb} and R_{bb} and the fractional rms returning to the values observed in Phase “1”. However, Phase “4” cannot be considered as a carbon copy of Phase “1”, mostly because of a much lower contribution from the disk at this stage with respect to the rising hard state. While Epochs 31 and 32 are characterised by a cold ($kT_{\text{disk}} \sim 0.3$ keV) disk, whose inner radius is unfortunately very loosely constrained, in the last two Epochs, the contribu-

tion from both the disk and the reflection components were not found to be statistically required by the fit. We suggest that as the source moves towards quiescence, the disk recedes and cools down significantly. This scenario is consistent with the observed X-ray spectral properties of the source in quiescence, where the source spectrum consists of thermal emission from the NS surface and often a non-negligible contribution from a non-thermal, power-law component of debated origin (e.g. Coti Zelati et al. 2014; Waterhouse et al. 2016; Ootes et al. 2018; Marino et al. 2018).

5. Conclusions

In this manuscript, we have presented an analysis of an extensive X-ray (including *Einstein Probe*, *NICER*, *NuSTAR*) and optical/UV (*LCO*, *Swift*) campaign targeting the archetypal NS LMXB Aql X-1 during its 2024 bright outburst. Our results allow us to estimate the time-scales for the rise-phase of the outburst, in particular the start time for the outburst at different electromagnetic bands, the optical-to-X-ray delay for the outburst early rise and the time required to transition from the hard to the soft state. Additionally, with spectral-timing analysis, we were able to reconstruct in detail the evolution of the main physical parameters of the accretion flow throughout the event. Our main conclusions are the following:

- By implementing both Gaussian Processes and a phenomenological analysis, we found MJD 60652 to be the approximate start time in the optical band of the 2024 outburst. Taking advantage of the soft X-rays sensitivity of WXT onboard EP, we found that the start time in the X-ray band had to occur some time between MJDs 60652 and 60655. We therefore suggest an optical-to-X-ray delay of 3 days or lower.
- During its 50-day outburst, Aql X-1 displayed all the three canonical XRB spectral states: the hard, intermediate, and soft states. Throughout the outburst, the spectra are well described by three main components: a disk blackbody, an additional blackbody likely coming from the NS surface and Compton-scattered by a hot inner flow or corona and a reflection component.
- Our spectral analysis provided estimates on the main spectral parameters during both the hard and soft states, tracing their evolution throughout the outburst. In particular: the electron temperature of the hot corona goes from ~ 23 keV to ~ 3 keV; the temperatures of the hot spot and disk go from ~ 0.6 to ~ 1.6 keV and from ~ 0.3 to ~ 0.9 keV, respectively; the black body size shrinks from an initial value of ~ 11 km to a final range between ~ 3 - 8 km in the soft state; the inner radius of the disk goes from an initial value of about ~ 60 - 100 km to ~ 10 km (although these values are likely underestimated).
- Along with the spectral parameters, the fractional rms also shows a significant change between the two states, going from an initial ~ 30 - 40% to $\lesssim 10\%$ in the soft state.
- Two different `relxill` code (García et al. 2013) versions were used to model the reflection component, `relxillCp` in the hard and `relxillNS` in the soft state, consistently with the expected drastic evolution of the Comptonization component spectral shape in the two states.
- Our dense monitoring covered with almost unprecedented detail the hard-to-soft transition, occurred between MJD 60581.5 and 60582, indicating it happened within a time window of approximately just 12 hours.

- We observed a peculiar increasing trend in the disk normalization during the day leading up to the hard-to-soft transition. While such an evolution could suggest a fluctuation of the inner disk edge around the transition, we suggest an alternative scenario where as the mass-accretion rate increases, a geometrically thicker BL forms. In this scenario, the increase in normalization reflects the increase in the emitting area of a disk “puffed up” because of an increasing contribution by advection.

LMXBs have been extensively studied for decades, yet we still poorly understand the physical mechanisms driving the onset and the evolution of their outbursts, and the role, if any, that the nature of the accreting star plays in this context. In this work, we have for the first time monitored the early phase of an outburst by Aql X-1, capturing the source at X-ray luminosity of less than 10^{35} erg s $^{-1}$. In the EP era, LMXB outbursts will be identified at analogously low luminosities, providing not only dense X-ray monitoring of the early outbursts’ rise but also the chance to trigger follow-up observations at other wavelengths, such as radio or optical, in this regime. Future multi-band campaigns driven by EP have the chance to open a new window on the behaviour of LMXBs at low accretion rates, thereby increasing our understanding of the accretion history of these sources.

Acknowledgements. We thank V. Grinberg for useful discussion. This work makes use of observations from the Las Cumbres Observatory global telescope network. AM, EP, FCZ and NR are supported by a ERC Consolidator Grant “MAGNESIA” under grant agreement No. 817661 (PI: Rea) and the National Spanish grant PID2023-153099NA-I00 (PI: Coti Zelati). FCZ is supported by a Ramón y Cajal fellowship (grant agreement RYC2021-030888-I). Y.C. acknowledges support from the grant RYC2021-032718-I, financed by MCIN/AEI/10.13039/501100011033 and the European Union NextGenerationEU/PRTR. NR is also supported by a ERC Proof of Concept Grant “DeepSpacePulse” under grant agreement No. 101189496 (PI: Rea). MCB acknowledges support from the INAF-Astrofit fellowship. This work was also partially supported by the program Unidad de Excelencia María de Maeztu CEX2020-001058-M. DMR is supported by Tamkeen under the NYU Abu Dhabi Research Institute grant CASS. YFH is supported by the National Key R&D Program of China (2021YFA0718500) and by the Xinjiang Tianchi Program. GZ acknowledges support from the China Manned Space Program with grant No. CMS-CSST-2025-A13.

Cavecchi, Y., Galloway, D., Heger, A., et al. 2025, arXiv e-prints, arXiv:2506.11966

Chambers, K. C., Magnier, E. A., Metcalfe, N., et al. 2016, arXiv e-prints, arXiv:1612.05560

Cheng, H., Zhang, C., Ling, Z., et al. 2025, Experimental Astronomy, 60, 15

Chevalier, C. & Illovaiky, S. A. 1991, A&A, 251, L11

Churazov, E., Gilfanov, M., & Revnivtsev, M. 2001, MNRAS, 321, 759

Coti Zelati, F., Campana, S., D’Avanzo, P., & Melandri, A. 2014, MNRAS, 438, 2634

Di Salvo, T., Papitto, A., Marino, A., Iaria, R., & Burderi, L. 2023, in Handbook of X-ray and Gamma-ray Astrophysics, 147

Di Salvo, T. & Sanna, A. 2022, in Astrophysics and Space Science Library, Vol. 465, Astrophysics and Space Science Library, ed. S. Bhattacharyya, A. Papitto, & D. Bhattacharya, 87–124

Di Salvo, T., Sanna, A., Burderi, L., et al. 2019, MNRAS, 483, 767

Díaz Trigo, M., Altamirano, D., Dincer, T., et al. 2018, A&A, 616, A23

Done, C., Gierliński, M., & Kubota, A. 2007, A&A Rev., 15, 1

Dunn, R. J. H., Fender, R. P., Körding, E. G., Belloni, T., & Cabanac, C. 2010, MNRAS, 403, 61

Esin, A. A., McClintock, J. E., & Narayan, R. 1997, ApJ, 489, 865

Ester, M., Kriegel, H.-P., Sander, J., & Xu, X. 1996, in Second International Conference on Knowledge Discovery and Data Mining (KDD’96). Proceedings of a conference held August 2–4, ed. D. W. Pfister & J. K. Salmon, 226–331

Fabian, A. C., Rees, M. J., Stella, L., & White, N. E. 1989, MNRAS, 238, 729

Fender, R. & Belloni, T. 2004, ARA&A, 42, 317

Fender, R. P., Homan, J., & Belloni, T. M. 2009, MNRAS, 396, 1370

Gaia Collaboration. 2020, VizieR Online Data Catalog: Gaia EDR3 (Gaia Collaboration, 2020), VizieR On-line Data Catalog: I/350. Originally published in: 2021A&A...649A...1G

Galloway, D. K., Munoz, M. P., Hartman, J. M., Psaltis, D., & Chakrabarty, D. 2008, ApJS, 179, 360

García, J., Dauser, T., Lohfink, A., et al. 2014, ApJ, 782, 76

García, J., Dauser, T., Reynolds, C. S., et al. 2013, ApJ, 768, 146

García, J. A., Dauser, T., Ludlam, R., et al. 2022, ApJ, 926, 13

Goodwin, A. J., Russell, D. M., Galloway, D. K., et al. 2020, MNRAS, 498, 3429

Grollimund, N., Corbel, S., Fender, R., & Motta, S. 2024, The Astronomer’s Telegram, 16888, 1

Güver, T., Boztepe, T., Ballantyne, D. R., et al. 2022, MNRAS, 510, 1577

Hameury, J. M. 2020, Advances in Space Research, 66, 1004

Hameury, J. M., Lasota, J. P., McClintock, J. E., & Narayan, R. 1997, ApJ, 489, 234

Heinke, C. O., Zheng, J., Maccarone, T. J., et al. 2025, ApJS, 279, 57

Henden, A. A., Levine, S., Terrell, D., et al. 2018, in American Astronomical Society Meeting Abstracts, Vol. 232, American Astronomical Society Meeting Abstracts #232, 223.06

Homan, J., Wijnands, R., van der Klis, M., et al. 2001, ApJS, 132, 377

Huppenkothen, D., Bachetti, M., Stevens, A. L., et al. 2019, apj, 881, 39

Illiano, G., Papitto, A., Marino, A., et al. 2024, A&A, 691, A189

Inogamov, N. A. & Sunyaev, R. A. 1999, Astronomy Letters, 25, 269

Inogamov, N. A. & Sunyaev, R. A. 2010, Astronomy Letters, 36, 848

Jain, R. K., Bailyn, C. D., Orosz, J. A., McClintock, J. E., & Remillard, R. A. 2001, ApJ, 554, L181

Kaastra, J. S. & Bleeker, J. A. M. 2016, A&A, 587, A151

Koljonen, K. I. I., Russell, D. M., Corral-Santana, J. M., et al. 2016, MNRAS, 460, 942

Kubota, A., Ebisawa, K., Makishima, K., & Nakazawa, K. 2005, ApJ, 631, 1062

Kubota, A., Tanaka, Y., Makishima, K., et al. 1998, PASJ, 50, 667

Kunte, P. K., Durgaprasad, N., Gokhale, G. S., et al. 1973, Nature Physical Science, 245, 37

La Monaca, F., Di Marco, A., Coti Zelati, F., et al. 2025, A&A, 702, A101

Lang, D., Hogg, D. W., Mierle, K., Blanton, M., & Roweis, S. 2010, AJ, 139, 1782

Lasota, J.-P. 2001, New A Rev., 45, 449

Le Stum, S., Cangemi, F., Coleiro, A., et al. 2024, The Astronomer’s Telegram, 16843, 1

Lewis, F., Russell, D. M., Fender, R. P., Roche, P., & Clark, J. S. 2008, arXiv e-prints, arXiv:0811.2336

Lin, D., Remillard, R. A., & Homan, J. 2007, ApJ, 667, 1073

Liu, M. J., Xu, X. P., Liang, Y. F., et al. 2024, The Astronomer’s Telegram, 16821, 1

Ludlam, R. M. 2024, Ap&SS, 369, 16

Ludlam, R. M., Miller, J. M., Bachetti, M., et al. 2017, ApJ, 836, 140

Ludlam, R. M., Miller, J. M., Cackett, E. M., et al. 2016, ApJ, 824, 37

Maitra, D., & Bailyn, C. D. 2004, ApJ, 608, 444

Mandal, M. & Pal, S. 2024, The Astronomer’s Telegram, 16826, 1

Mandal, M., Pal, S., Jaisawal, G. K., et al. 2025, Journal of High Energy Astrophysics, 47, 100387

Marcel, G., Ferreira, J., Petrucci, P. O., et al. 2018, A&A, 615, A57

Marino, A., Anitra, A., Mazzola, S. M., et al. 2022, MNRAS, 515, 3838

Marino, A., Degenaar, N., Di Salvo, T., et al. 2018, MNRAS, 479, 3634

References

Aigrain, S. & Foreman-Mackey, D. 2023, ARA&A, 61, 329

Alabarta, K., Russell, D. M., Rout, S. K., et al. 2025, The Astronomer’s Telegram, 17321, 1

Anitra, A., Di Salvo, T., Iaria, R., et al. 2021, A&A, 654, A160

Arnaud, K., Dorman, B., & Gordon, C. 1999, XSPEC: An X-ray spectral fitting package, Astrophysics Source Code Library

Babkovskaya, N., Brandenburg, A., & Poutanen, J. 2008, MNRAS, 386, 1038

Bachetti, M. & Huppenkothen, D. 2018, ApJ, 853, L21

Bachetti, M., Huppenkothen, D., Stevens, A., et al. 2024, Journal of Open Source Software, 9, 7389

Bachetti, M., Rana, V., Walton, D. J., et al. 2013, ApJ, 778, 163

Bahramian, A. & Degenaar, N. 2023, in Handbook of X-ray and Gamma-ray Astrophysics, 120

Banerjee, S. & Homan, J. 2024, MNRAS, 529, 4311

Bernardini, F., Russell, D. M., Koljonen, K. I. I., et al. 2016, ApJ, 826, 149

Bertin, E. & Arnouts, S. 1996, A&AS, 117, 393

Böck, M., Grinberg, V., Pottschmidt, K., et al. 2011, A&A, 533, A8

Bramich, D. M. & Freudling, W. 2012, MNRAS, 424, 1584

Burke, M. J., Gilfanov, M., & Sunyaev, R. 2017, MNRAS, 466, 194

Buxton, M. M. & Bailyn, C. D. 2004, ApJ, 615, 880

Cackett, E. M., Fridriksson, J. K., Homan, J., Miller, J. M., & Wijnands, R. 2011, MNRAS, 414, 3006

Campana, S., Brivio, F., Degenaar, N., et al. 2014, MNRAS, 441, 1984

Campana, S., Stella, L., Mereghetti, S., et al. 1998, ApJ, 499, L65

Casella, P., Altamirano, D., Patruno, A., Wijnands, R., & van der Klis, M. 2008, ApJ, 674, L41

Marino, A., Del Santo, M., Cocchi, M., et al. 2019, MNRAS, 490, 2300

Marino, A., Russell, T. D., Del Santo, M., et al. 2023, MNRAS, 525, 2366

Mata Sánchez, D., Muñoz-Darias, T., Casares, J., & Jiménez-Ibarra, F. 2017, MNRAS, 464, L41

Matsuoka, M., Kawasaki, K., Ueno, S., et al. 2009, PASJ, 61, 999

Mineshige, S., Hirano, A., Kitamoto, S., Yamada, T. T., & Fukue, J. 1994, ApJ, 426, 308

Miyamoto, S., Kitamoto, S., Hayashida, K., & Egoshi, W. 1995, ApJ, 442, L13

Muñoz-Darias, T., Fender, R. P., Motta, S. E., & Belloni, T. M. 2014, MNRAS, 443, 3270

Narayan, R. & Yi, I. 1995, ApJ, 452, 710

Niwano, M., Murata, K. L., Ito, N., Yatsu, Y., & Kawai, N. 2023, MNRAS, 525, 4358

Ootes, L. S., Wijnands, R., Page, D., & Degenaar, N. 2018, MNRAS, 477, 2900

Orosz, J. A., Remillard, R. A., Bailyn, C. D., & McClintock, J. E. 1997, ApJ, 478, L83

Osaki, Y. 1974, PASJ, 26, 429

Pedregosa, F., Varoquaux, G., Gramfort, A., et al. 2011, Journal of Machine Learning Research, 12, 2825

Pintore, F., Pinto, C., Rodriguez-Castillo, G., et al. 2025, A&A, 695, A238

Poole, T. S., Breeveld, A. A., Page, M. J., et al. 2008, MNRAS, 383, 627

Popham, R. & Sunyaev, R. 2001, ApJ, 547, 355

Poutanen, J. & Veledina, A. 2014, Space Sci. Rev., 183, 61

Poutanen, J., Veledina, A., & Zdziarski, A. A. 2018, A&A, 614, A79

Putha, K. G., Bhargava, Y., & Bhattacharyya, S. 2024, MNRAS, 532, 3961

Ren, X. Q., Wang, Y., Zhang, S. N., et al. 2022, ApJ, 932, 66

Roming, P. W. A., Kennedy, T. E., Mason, K. O., et al. 2005, Space Sci. Rev., 120, 95

Rout, S. K., Alabarta, K., Marino, A., et al. 2025a, The Astronomer's Telegram, 17336, 1

Rout, S. K., Alabarta, K., Russell, D. M., et al. 2024, The Astronomer's Telegram, 16822, 1

Rout, S. K., Baglio, M. C., Hughes, A. K., et al. 2025b, ApJ, 988, 153

Rout, S. K., Muñoz-Darias, T., Homan, J., et al. 2025c, ApJ, 978, 12

Russell, D. M., Bramich, D. M., Lewis, F., et al. 2019, Astronomische Nachrichten, 340, 278

Russell, T. D., Fijma, S., Degenaar, N., et al. 2024, The Astronomer's Telegram, 16823, 1

Saavedra, E. A., García, F., Fogantini, F. A., et al. 2023, MNRAS, 522, 3367

Shahbaz, T., Bandyopadhyay, R. M., Charles, P. A., et al. 1998, MNRAS, 300, 1035

Shakura, N. I. & Sunyaev, R. A. 1973, A&A, 24, 337

Shimura, T. & Takahara, F. 1995, ApJ, 445, 780

Stetson, P. B. 1990, PASP, 102, 932

Suleimanov, V. & Poutanen, J. 2006, MNRAS, 369, 2036

Sun, H., Zhang, M. H., Cheng, H. Q., et al. 2025, GRB Coordinates Network, 40375, 1

Tetarenko, B. E., Sivakoff, G. R., Heinke, C. O., & Gladstone, J. C. 2016, ApJS, 222, 15

Torrey, J. L., Denneau, L., Flewelling, H., et al. 2018, ApJ, 867, 105

Tucker, M. A., Shappee, B. J., Holoiien, T. W. S., et al. 2018, ApJ, 867, L9

Tudose, V., Fender, R. P., Linares, M., Maitra, D., & van der Klis, M. 2009, MNRAS, 400, 2111

van der Klis, M. 2004, arXiv e-prints, astro

Verner, D. A., Ferland, G. J., Korista, K. T., & Yakovlev, D. G. 1996, ApJ, 465, 487

Šimon, V. 2002, A&A, 381, 151

Wang, Y. L., Zhang, W. J., Wang, W. X., Liu, Y., & Einstein Probe Team. 2025, The Astronomer's Telegram, 17013, 1

Waterhouse, A. C., Degenaar, N., Wijnands, R., et al. 2016, MNRAS, 456, 4001

Wijnands, R. & van der Klis, M. 1999, ApJ, 514, 939

Wilms, J., Allen, A., & McCray, R. 2000, ApJ, 542, 914

Xu, X. P., Wang, Y., Zhou, H., et al. 2024, The Astronomer's Telegram, 16714, 1

Yan, Z., Zhang, G., Chen, Y.-P., et al. 2025, Research in Astronomy and Astrophysics, 25, 045005

Yuan, W., Dai, L., Feng, H., et al. 2025, Science China Physics, Mechanics, and Astronomy, 68, 239501

Zdziarski, A. A. & De Marco, B. 2020, ApJ, 896, L36

Zdziarski, A. A., De Marco, B., Szanecki, M., Niedźwiecki, A., & Markowitz, A. 2021a, ApJ, 906, 69

Zdziarski, A. A., Dziełak, M. A., De Marco, B., Szanecki, M., & Niedźwiecki, A. 2021b, ApJ, 909, L9

Zdziarski, A. A., Gierliński, M., Mikołajewska, J., et al. 2004, MNRAS, 351, 791

Zdziarski, A. A., Szanecki, M., Poutanen, J., Gierliński, M., & Biernacki, P. 2020, MNRAS, 492, 5234

Zhang, W., Jahoda, K., Kelley, R. L., et al. 1998, ApJ, 495, L9

Zurita, C., Torres, M. A. P., Steeghs, D., et al. 2006, ApJ, 644, 432

¹ Institute of Space Sciences (ICE, CSIC), Campus UAB, Carrer de Can Magrans s/n, E-08193 Barcelona, Spain

² Institut d'Estudis Espacials de Catalunya (IEEC), 08860 Castelldefels (Barcelona), Spain

³ INAF/IASF Palermo, via Ugo La Malfa 153, I-90146 - Palermo, Italy

⁴ INAF–Osservatorio Astronomico di Brera, Via Bianchi 46, I-23807 Merate (LC), Italy

⁵ Center for Astrophysics and Space Science (CASS), New York University Abu Dhabi, PO Box 129188, Abu Dhabi, UAE

⁶ Departament de Física, EEBE, Universitat Politècnica de Catalunya, Av. Eduard Maristany 16, 08019 Barcelona, Spain

⁷ Dipartimento di Fisica e Chimica - Emilio Segrè, Università di Palermo, via Archirafi 36 - 90123 Palermo, Italy

⁸ Eureka Scientific, Inc., 2452 Delmer Street, Oakland, CA 94602, USA

⁹ School of Physics and Astronomy, Sun Yat-sen University, Zhuhai, 519082, People's Republic of China

¹⁰ INAF – Osservatorio Astrofisico di Torino, Strada Osservatorio 20, I-10025 Pino Torinese, Italy

¹¹ Sydney Institute for Astronomy, School of Physics A28, The University of Sydney, Sydney, NSW 2006, Australia

¹² School of Astronomy and Space Science, University of Chinese Academy of Sciences, 19A Yuquan Road, Beijing 100049, China

¹³ National Astronomical Observatories, Chinese Academy of Sciences, 20A Datun Road, Beijing 100101, China

¹⁴ Dipartimento di Fisica, Università degli Studi di Cagliari, SP Monserrato-Sestu, KM 0.7, Monserrato, 09042 Italy

¹⁵ Key Laboratory of Particle Astrophysics, Institute of High Energy Physics, Chinese Academy of Sciences, Beijing 100049, People's Republic of China

¹⁶ Anton Pannekoek Institute for Astronomy, University of Amsterdam, Science Park 904, 1098 XH, Amsterdam, the Netherlands

¹⁷ ESO, Karl-Schwarzschild-Strasse 2, D-85748 Garching bei München, Germany

¹⁸ IRAP, CNRS, 9 avenue du Colonel Roche, BP 44346, 31028 Toulouse Cedex 4, France;

¹⁹ School of Astronomy and Space Science, Nanjing University, Nanjing 210023, China

²⁰ Key Laboratory of Modern Astronomy and Astrophysics (Nanjing University), Ministry of Education, Nanjing 210023, China

²¹ Faulkes Telescope Project, School of Physics and Astronomy, Cardiff University, The Parade, Cardiff, CF24 3AA, Wales, UK

²² The Schools' Observatory, Astrophysics Research Institute, Liverpool John Moores University, 146 Brownlow Hill, Liverpool UK

²³ Purple Mountain Observatory, Chinese Academy of Sciences, Nanjing 210023, China

²⁴ School of Astronomy and Space Sciences, University of Science and Technology of China, Hefei 230026, China

²⁵ School of Physics and Astronomy, University of Southampton, Southampton, SO17 1BJ, UK

²⁶ Scuola Universitaria Superiore IUSS Pavia, Piazza della Vittoria 15, I-27100, Pavia, Italy

²⁷ European Space Agency (ESA), European Space Astronomy Centre (ESAC), Camino Bajo del Castillo s/n, E-28692 Villanueva de la Cañada, Madrid, Spain

²⁸ Department of Astronomy, Yale University, PO Box 208101, New Haven, CT 06520-8101, USA

²⁹ Yunnan Observatories, Chinese Academy of Sciences, Kunming 650216, People's Republic of China

³⁰ Department of Physics, The University of Hong Kong, Pokfulam Road, Hong Kong

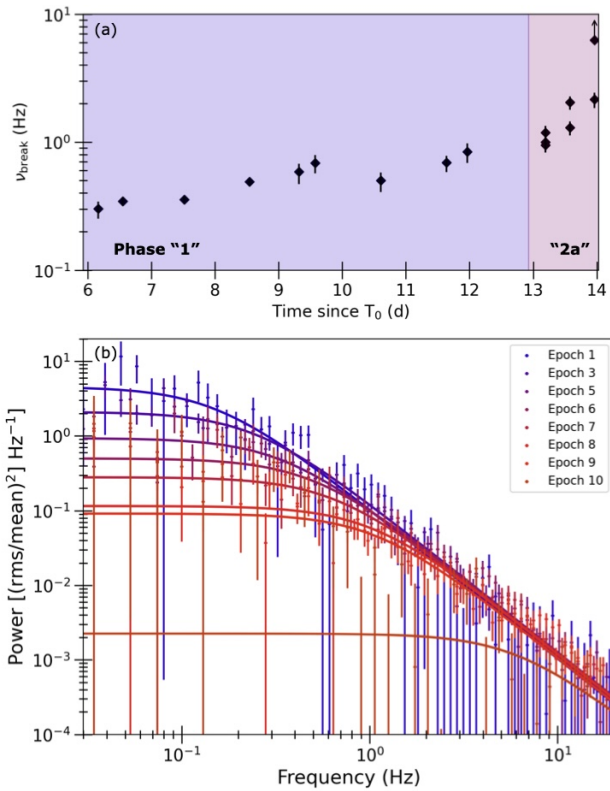


Fig. A.1. Panel (a): evolution of the break frequency ν_{break} throughout the hard to intermediate states in Aql X-1, obtained from the analysis of single *NICER* PDS spectra; panel (b) selected PDS and best-fit single Lorentzian models, showing the increase in ν_{break} over time.

Appendix A: Tables and additional figures

In this Section, we report details and results of this work in several Tables and Figures. In particular, Table A.1 lists all the (X-ray) observations and illustrates the Epochs classification we adopted, Table A.2 reports the results of the phenomenological analysis explained in Section 3.1, Table A.3 shows the results of the fit to the broadband *NICER* +*NuSTAR* spectra in Epochs 3 and 28, while Table A.4 reports the spectral analysis on each individual Epoch (more details in Section 3.2). Finally, the evolution of ν_{break} through the hard and hard-intermediate states (Phases “1” and “2a”), obtained through the analysis described in Section 3.3, is displayed in Fig. A.1.

Appendix B: Early rise analysis with Gaussian Processes

We adopted the implementation provided in the `scikit-learn` library (Pedregosa et al. 2011), using a kernel composed of a constant term multiplied by a Matérn kernel with smoothness parameter $\nu = 1.5$, and added a white-noise component to account for measurement uncertainties. This configuration offers sufficient flexibility to capture both smooth trends and stochastic intrinsic variability.

We applied the Gaussian Process (GP) regression separately to the X-ray light curves from EP/WXT (0.5–4 keV) and *MAXI* (3–20 keV), as well as to the *LCO* optical data. To incorporate the two early EP/WXT upper limits without biasing the model, we introduced “pseudo-measurements” at half the reported upper-limit values, with uncertainties equal to half those values. This approach encodes the one-sided nature of the non-detections

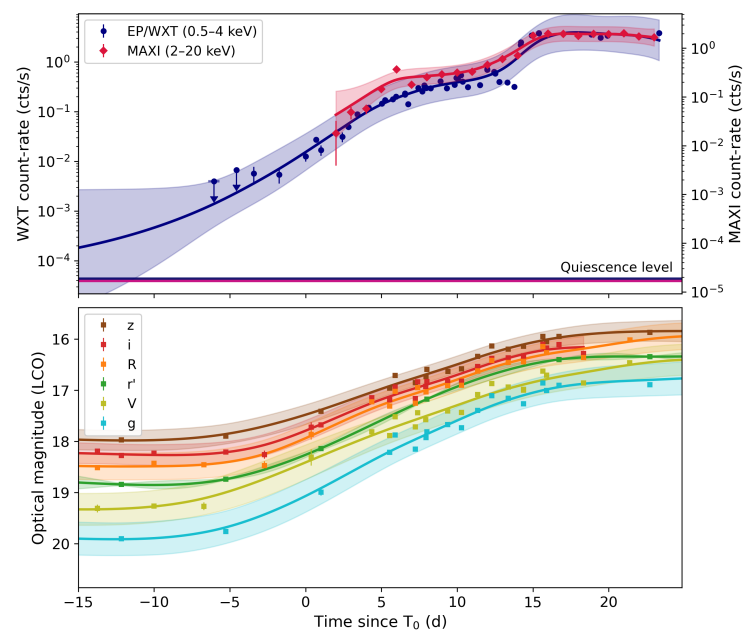


Fig. B.1. Multi-band light curves of Aql X-1 during the rise to outburst, spanning X-ray (top panel) and optical (bottom panel) observations, along with their respective GP fits and 1σ confidence intervals. In the top panel, the quiescent level is marked for both EP/WXT and *MAXI* for reference.

with a conservative 1σ error while preventing the GP model from being over-constrained.

Figure B.1 shows the GP models overlaid on the data, highlighting the outburst onset and early evolution across energy bands. We estimate the onset of the outburst in the soft X-rays as the latest time at which the outburst could have plausibly begun, identified as the last intersection between the upper bound of the 95% confidence interval from the EP/WXT GP model and the estimated quiescent level, as determined via backward extrapolation. Based on this criterion, the enhanced X-ray activity likely began earlier than approximately MJD 60557, at $T_0 - 10$ d.

Also in this case, the above estimate relies on the smooth extrapolation provided by the GP model. Since the earliest EP/WXT measurements are upper limits, a sharp steepening or discontinuity in the X-ray flux just before the first detection cannot be excluded a priori. In that case, the actual outburst onset could have occurred later than inferred. Our estimate should therefore be interpreted under the assumption of a continuous rise and therefore as a lower limit for the true start of the outburst in the X-ray band.

Appendix C: Spectral analysis with `diskpbb`

In order to explore the possibility of a boundary layer formation during the spectral state transition in Aql X-1, we have tested whether `diskpbb` might serve as a temporary replacement for `diskbb` for Epochs 6 to 9, where an odd increase in normalization was observed (see Discussion). For each of these Epochs, we have used the best-fit model identified in Section 3.2, “H” (until Epoch 9) or “S” (Epoch 10), but replaced `diskbb` with `diskpbb` and re-run the fits. An initial attempt at running the fit with the radial temperature index p as a free parameter was inconclusive, as the number of degeneracies in the fit prevented us from constraining this parameter. We therefore opted for a different approach, launching multiple fits with p fixed to values

Table A.1. Table of the X-ray observations used in this work. †: The observation has been split into segments because of intra-observational variability. All the EP/FXT observations used in this work were performed in TM mode.

Observation ID	Telescope/Instrument	Observation start (MJD)	Observation start (UTC)	Exposure (ks)	Epoch
7050340101	NICER	60573.664	2024-09-20 15:55:57.184	1.7	
7050340102	NICER	60574.049	2024-09-21 01:11:14.184	3.7	Epoch 1
06800000116	EP/FXT	60574.067	2024-09-21 01:36:54.067	4.2	
7050340103	NICER	60575.015	2024-09-22 00:20:58.184	5.5	
06800000119	EP/FXT	60575.337	2024-09-22 08:04:53.088	5.5	Epoch 2
91001338002	NuSTAR	60576.591	2024-09-23 14:10:48.684	18.3	
7050340104	NICER	60576.045	2024-09-23 01:04:16.184	4.1	
7675010101	NICER	60576.818	2024-09-23 19:37:59.184	0.6	Epoch 3
7050340105	NICER	60577.012	2024-09-24 00:17:03.184	0.3	
7675010102	NICER	60577.077	2024-09-24 01:51:11.184	0.9	
06800000122	EP/FXT	60577.755	2024-09-24 18:07:28.974	3.5	Epoch 4
7675010103	NICER	60578.560	2024-09-25 13:27:02.184	0.2	
7050340107	NICER	60579.141	2024-09-26 03:23:19.184	1.2	
7675010104	NICER	60579.464	2024-09-26 11:07:55.184	1.0	Epoch 5
06800000124	EP/FXT	60579.479	2024-09-26 11:29:09.069	4.9	
7675010105	NICER	60580.045	2024-09-27 01:04:11.184	0.3	
7050340108†	NICER	60580.690	2024-09-27 16:33:25.702	1.0	
7050340108†	NICER	60580.755	2024-09-27 18:06:43.184	1.0	Epoch 6
7050340108†	NICER	60580.883	2024-09-27 21:12:08.184	0.9	
7675010106†	NICER	60581.077	2024-09-28 01:51:10.337	0.6	Epoch 7
7675010106†	NICER	60581.335	2024-09-28 08:02:50.184	1.0	Epoch 8
7050340109†	NICER	60581.465	2024-09-28 11:08:58.389	0.8	Epoch 9
7050340109†	NICER	60581.668	2024-09-28 16:02:08.184	0.2	Epoch 10
06800000125†	EP/FXT	60581.692	2024-09-28 16:37:05.989	2.2	Epoch 11
06800000125†	EP/FXT	60581.761	2024-09-28 18:15:44.977	2.0	Epoch 12
7050340109†	NICER	60581.916	2024-09-28 21:59:17.184	1.9	Epoch 13
7050340110†	NICER	60582.240	2024-09-29 05:45:49.069	0.8	Epoch 14
7675010107†	NICER	60582.368	2024-09-29 08:49:21.367	1.1	Epoch 15
7675010107†	NICER	60582.626	2024-09-29 15:01:16.184	1.0	Epoch 16
7050340110†	NICER	60582.755	2024-09-29 18:06:54.184	1.0	Epoch 17
7050340110†	NICER	60582.834	2024-09-29 20:00:37.184	1.1	Epoch 18
7050340111†	NICER	60583.077	2024-09-30 01:51:32.191	0.4	Epoch 19
7050340111†	NICER	60583.207	2024-09-30 04:57:53.184	2.4	
7675010108	NICER	60583.400	2024-09-30 09:36:15.184	2.2	Epoch 20
7675010109	NICER	60584.756	2024-10-01 18:08:04.184	2.1	Epoch 21
7050340113	NICER	60585.014	2024-10-02 00:20:10.184	1.7	Epoch 22
7675010110	NICER	60585.853	2024-10-02 20:28:14.184	2.0	Epoch 23
7675010111	NICER	60586.305	2024-10-03 07:18:38.184	2.2	Epoch 24
7050340114	NICER	60586.692	2024-10-03 16:36:43.184	1.2	
7675010112	NICER	60587.209	2024-10-04 05:01:14.184	1.3	Epoch 25
7675010113	NICER	60588.437	2024-10-05 10:28:45.184	2.2	Epoch 26
7675010118	NICER	60593.413	2024-10-10 09:54:11.184	0.4	Epoch 27
7675010119	NICER	60594.123	2024-10-11 02:57:47.184	0.4	
91001345002	NuSTAR	60602.114	2024-10-19 02:43:53.684	20.1	Epoch 28
7675010133	NICER	60616.708	2024-11-02 16:59:05.184	1.0	
7675010134	NICER	60617.096	2024-11-03 02:18:23.184	1.9	Epoch 29
7050340124	NICER	60618.513	2024-11-04 12:19:21.184	1.9	Epoch 30
7675010135	NICER	60621.090	2024-11-07 02:10:00.184	2.2	Epoch 31
7675010136	NICER	60622.187	2024-11-08 04:28:51.184	1.5	Epoch 32
7675010137	NICER	60623.154	2024-11-09 03:42:11.184	2.1	Epoch 33

Table A.2. Results of the multi-band light curves analysis (see Section 3.1 for more details). All times are reported with respect to $T_0 = 60567.5$ MJD. \ddagger : nominal bands from Poole et al. (2008)

Multi-band phenomenological analysis						
Instrument/Filter	Energy range	A_X (cts/s)	f_X (Broken exponential)		$T_{\text{start},X}$ (d)	T_{knee} (d)
	(keV)		α_1	α_2		
EP/WXT	0.5-4	0.0150 ± 0.0012	-0.50 ± 0.02	-0.121 ± 0.003	>-11.0	4.9 ± 0.1
MAXI	3-20	0.004 ± 0.003	-0.70 ± 0.14	-0.050 ± 0.017	>-6.1	5.7 ± 0.3
	(Å)		mag_{opt} (Piecewise linear)		$T_{\text{start},\text{opt}}$ (d)	
LCO/z'	7660-9740		17.920 ± 0.009	-0.0970 ± 0.0021	-5.1 ± 0.3	
LCO/i'	6255-8835		18.200 ± 0.008	-0.1068 ± 0.0015	-4.5 ± 0.2	
LCO/R	4827-7987		18.42 ± 0.02	-0.1140 ± 0.0017	-4.5 ± 0.3	
LCO/r'	4825-7605		18.770 ± 0.009	-0.140 ± 0.004	-3.6 ± 0.3	
LCO/V	4608-6288		19.26 ± 0.04	-0.130 ± 0.003	-6.0 ± 0.4	
LCO/g'	3270-6270		19.73 ± 0.02	-0.150 ± 0.003	-4.5 ± 0.3	
	(Å) ‡		mag_{opt} (Simple linear)		a_{UV}	
UVOT/B	3417-5367				-0.11 ± 0.02	
UVOT/V	4699-6237				-0.11 ± 0.02	

between 0.55 and 0.75 in steps of 0.05, where $p = 0.75$ corresponds to the standard thin-disk model of Shakura & Sunyaev (1973). All fits are acceptable and comparable to the ones obtained with `diskbb`, as expected due to the degeneracies in the model used, with the exception of Epoch 10, for which using `diskpbb` with p lower than 0.65 worsened the fit significantly. We show the evolution of kT_{bb} , R_{bb} , kT_{disk} and R_{disk} in Fig. C.1. As evident from the plot, for all values of p we retrieve the same trend for both parameters, with the radius (temperature) initially increasing (decreasing) to then decrease (increase) again. However, a clear correlation exists between the values of p and both R_{bb} and R_{disk} . If we therefore allow p to slowly decrease from the initial thin-disk value (0.75) to a slightly lower value (0.55), we obtain an acceptable description of the spectra by keeping R_{disk} and R_{bb} fixed or even allowing them to decrease.

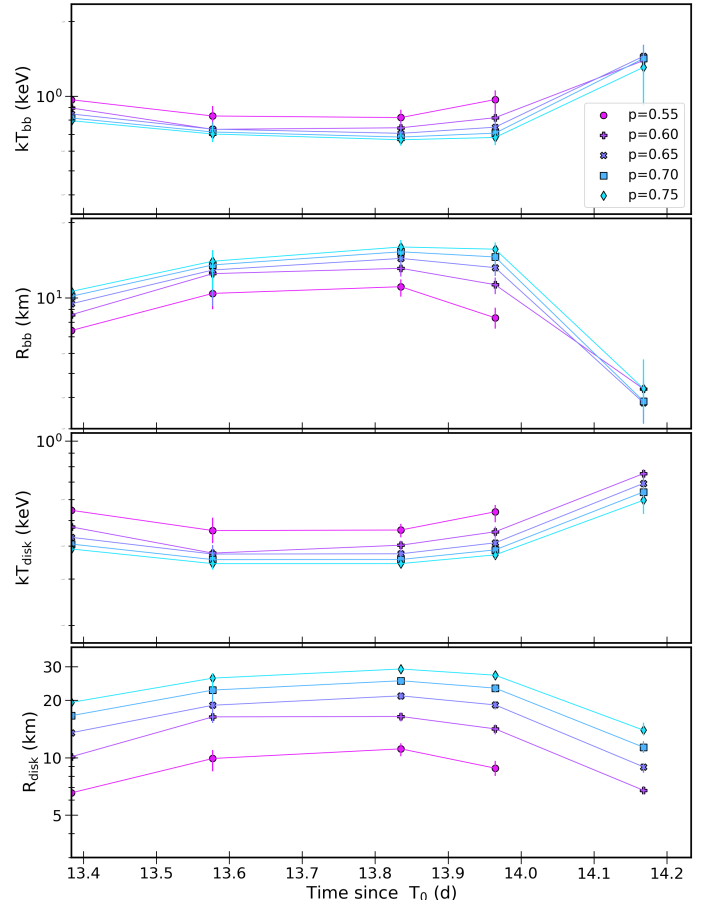


Fig. C.1. Evolution of best-fit kT_{bb} , R_{bb} , kT_{disk} and R_{disk} for Epochs 6 to 10 using the `diskpbb` model and fixing the parameter p to several values, going from 0.75 (classical Shakura & Sunyaev 1973 disk, negligible energy losses through advection) to 0.5 (“slim” disk, significant part of the energy lost through advection).

Table A.3. Results of the broadband spectral analysis. Quoted errors reflect 90% confidence level. The parameters that were kept frozen during the fits are reported between round parentheses. R_G represents the gravitational radius. The reported flux values correspond to the 1–10 keV energy range. †: estimated from the parameter normalization and likely underestimated (see text for more details).

Broadband spectral analysis					
Component	Parameters		Description	Epoch 3	Epoch 27
constant	c_{cal}		Intercalibration constant	(1.0)	
TBabs	N_H	10^{22} cm^{-2}	Equivalent hydrogen column density	(0.50)	
thComp	Γ		Power-law index of the Comptonization spectrum	1.85 ± 0.01	$3.3_{-0.2}^{+0.3}$
	kT_e	keV	Electron temperature of the corona	23_{-1}^{+2}	$3.4_{-0.2}^{+0.3}$
	f_{cov}		Covering fraction	(1.0)	
bbodyrad	kT_{bb}	keV	Blackbody temperature	$0.72_{-0.02}^{+0.03}$	$1.50_{-0.03}^{+0.06}$
	R_{bb}	km	Blackbody radius [†]	$11.1_{-0.8}^{+0.7}$	$4.4_{-0.4}^{+0.2}$
diskbb	kT_{disk}	keV	Inner disk temperature	0.38 ± 0.02	$0.93_{-0.04}^{+0.05}$
	R_{disk}	(km)	Disk inner radius [†]	$14.4_{-0.6}^{+0.8}$	$8.9_{-0.8}^{+1.0}$
expabs	$E_{\text{cut-off,low}}$	keV	Low energy cut-off	$=3 \times kT_{\text{bb}}$	-
relxillCp	i	°	System inclination	30 ± 2	-
	a^*		Spin parameter	(0)	-
	R_{in}	R_G	Inner disk radius	< 8.0	-
	R_{out}	R_G	Outer disk radius	(1000)	-
	ϵ		Disk emissivity	(3.0)	-
	z		Redshift to the source	(0)	-
	Γ_{relxill}		Power-law index of the incident spectrum	$=\Gamma$	-
	$\log \xi$		Disk ionization	$3.00_{-0.12}^{+0.10}$	-
	$\log N$	cm^{-3}	Disk density	(19.0)	-
	A_{Fe}		Fe abundance of reflecting material	(1.0)	-
relxillNS	$kT_{e,\text{refl}}$	keV	Electron temperature of the corona	$=kT_e$	-
	f_{refl}		Reflection fraction	(-1.0)	-
	K_{refl}	$(\times 10^{-3})$	Reflection normalization	2.30 ± 0.17	-
	i	°	System inclination	-	31 ± 2
	a^*		Spin parameter	-	(0)
	R_{in}	R_G	Inner disk radius	-	13_{-4}^{+5}
	R_{out}	R_G	Outer disk radius	-	(1000)
	ϵ		Disk emissivity	-	(3.0)
	z		Redshift to the source	-	(0)
	$kT_{\text{bb,relx}}$	keV	Blackbody temperature of the incident spectrum	-	$=kT_{\text{bb}}$
	$\log \xi$		Disk ionization	-	$3.01_{-0.06}^{+0.12}$
	$\log N$	cm^{-3}	Disk density	-	(19.0)
	A_{Fe}		Fe abundance of reflecting material	-	(1.0)
	$kT_{e,\text{refl}}$	keV	Electron temperature of the corona	-	$=kT_e$
	f_{refl}		Reflection fraction	-	(-1.0)
	K_{refl}	$(\times 10^{-3})$	Reflection normalization	-	$2.2_{-0.2}^{+0.3}$
cflux	$F_{1-10 \text{ keV}}$	$(\times 10^{-9}) \text{ erg cm}^{-2} \text{ s}^{-1}$	X-ray unabsorbed flux	2.290 ± 0.004	11.80 ± 0.01
	χ^2	(dof)		892(960)	298(309)

Table A.4. Results of the spectral analysis for each individual Epoch. A distance of 4.5 kpc has been assumed to estimate the X-ray luminosity in the 1-10 keV range, L_{10} . The parameters that were kept frozen during the fits are reported between round parentheses.

Epoch	Time (d)	N_H ($\times 10^{22}$)	Γ	kT_{bb} (keV)	R_{bb} (km)	kT_{disk} (keV)	R_{disk} (km)	K_{refl}	L_{10} ($\times 10^{36}$ erg/s)	χ^2 (d.o.f.)
1	60573.93	(0.500)	1.85 \pm 0.03	0.56 \pm 0.02	13.0 $^{+1.0}_{-0.9}$	0.20 \pm 0.02	50 $^{+14}_{-8}$	0.95 \pm 0.24	3.420 \pm 0.013	362(370)
2	60575.18	(0.500)	1.81 \pm 0.03	0.62 \pm 0.03	12.5 $^{+1.1}_{-1.0}$	0.30 \pm 0.02	24 $^{+5}_{-3}$	1.9 $^{+0.4}_{-0.3}$	4.890 \pm 0.013	181(226)
3	60576.69	(0.500)	1.850 $^{+0.011}_{-0.008}$	0.71 \pm 0.03	11.0 $^{+1.0}_{-0.8}$	0.40 \pm 0.02	14.4 $^{+0.8}_{-0.6}$	2.3 \pm 0.2	6.805 \pm 0.013	887(961)
4	60577.76	(0.500)	1.80 $^{+0.12}_{-0.10}$	0.60 \pm 0.09	15.0 $^{+6.0}_{-4.0}$	0.25 \pm 0.03	39 $^{+12}_{-6}$	4.0 $^{+1.9}_{-1.6}$	7.40 \pm 0.03	106(77)
5	60579.34	(0.500)	1.80 \pm 0.03	0.72 \pm 0.03	12.0 $^{+1.1}_{-0.9}$	0.35 \pm 0.01	19.5 \pm 0.9	4.4 \pm 0.5	8.95 \pm 0.03	568(590)
6	60580.78	(0.500)	1.80 \pm 0.03	0.75 \pm 0.04	12.5 $^{+1.3}_{-1.1}$	0.40 \pm 0.02	22.5 $^{+3}_{-1.1}$	2.0 $^{+1.1}_{-1.2}$	12.00 \pm 0.04	354(400)
7	60581.08	(0.500)	1.75 \pm 0.05	0.70 \pm 0.05	16 $^{+3}_{-2}$	0.34 \pm 0.02	29 $^{+3}_{-2}$	8.5 \pm 1.3	14.00 \pm 0.05	131(129)
8	60581.34	(0.500)	1.75 \pm 0.04	0.70 \pm 0.04	17.5 $^{+2.0}_{-1.7}$	0.35 \pm 0.01	32.5 $^{+1.3}_{-1.2}$	-	15.50 \pm 0.05	115(136)
9	60581.46	(0.500)	1.75 \pm 0.04	0.70 \pm 0.05	17.5 $^{+2.5}_{-2.0}$	0.35 \pm 0.01	30.1 $^{+1.3}_{-1.1}$	-	16.10 \pm 0.05	108(134)
10	60581.67	(0.500)	1.75 $^{+0.30}_{-0.20}$	1.30 $^{+0.40}_{-0.14}$	5.0 \pm 1.5	0.60 $^{+0.07}_{-0.02}$	15.5 $^{+0.8}_{-1.5}$	1.50 \pm 0.46	19.65 \pm 0.09	104(119)
11	60581.69	(0.500)	(1.600)	1.60 $^{+0.13}_{-0.13}$	3.0 $^{+3.0}_{-0.7}$	0.690 \pm 0.020	12.5 $^{+1.4}_{-0.4}$	2.4 $^{+0.8}_{-1.1}$	21.20 \pm 0.05	118(80)
12	60581.76	(0.500)	(1.600)	1.3 \pm 0.3	5.0 $^{+1.0}_{-1.4}$	0.75 \pm 0.06	11.5 $^{+1.4}_{-0.9}$	2.2 $^{+0.6}_{-0.9}$	26.70 \pm 0.06	91(83)
13	60581.92	(0.500)	2.5 $^{+0.4}_{-0.2}$	1.40 $^{+0.16}_{-0.13}$	5.5 $^{+1.5}_{-1.1}$	0.85 $^{+0.05}_{-0.04}$	11.0 $^{+0.6}_{-0.5}$	1.5 \pm 0.3	32.60 \pm 0.08	54(146)
14	60582.24	(0.500)	(3.100)	1.25 \pm 0.07	7.2 $^{+1.0}_{-0.9}$	0.80 \pm 0.04	11.5 \pm 0.6	1.2 \pm 0.3	35.80 \pm 0.10	83(140)
15	60582.37	(0.500)	3.5 $^{+2.0}_{-0.6}$	1.40 $^{+0.18}_{-0.14}$	7.0 $^{+1.9}_{-1.4}$	0.82 \pm 0.06	11.0 $^{+0.9}_{-0.8}$	1.6 \pm 0.5	41.50 \pm 0.11	71(140)
16	60582.63	(0.500)	(3.100)	1.30 \pm 0.07	8.0 \pm 1.0	0.80 $^{+0.05}_{-0.04}$	11.6 \pm 0.7	1.7 \pm 0.5	44.90 \pm 0.12	57(141)
17	60582.75	(0.509)	3.3 $^{+1.3}_{-0.4}$	1.34 $^{+0.17}_{-0.10}$	8.7 $^{+1.7}_{-1.8}$	0.79 \pm 0.08	12.0 $^{+1.0}_{-1.1}$	1.7 \pm 0.5	52.90 \pm 0.14	66(142)
18	60582.83	(0.500)	(3.100)	1.38 \pm 0.10	7.6 $^{+1.0}_{-1.2}$	0.87 \pm 0.07	10.3 \pm 0.7	2.0 $^{+0.4}_{-0.5}$	49.60 \pm 0.12	68(147)
19	60583.08	(0.500)	(3.100)	1.56 \pm 0.10	6.0 $^{+1.2}_{-0.8}$	0.92 \pm 0.06	9.7 $^{+0.8}_{-0.6}$	3.0 \pm 0.7	53.60 \pm 0.17	95(133)
20	60583.30	(0.500)	(3.100)	1.34 \pm 0.03	8.3 $^{+0.5}_{-0.5}$	0.82 \pm 0.03	11.3 \pm 0.4	1.7 \pm 0.3	49.20 \pm 0.11	124(302)
21	60584.76	(0.500)	(3.100)	1.35 \pm 0.07	7.8 $^{+0.8}_{-0.8}$	0.850 \pm 0.050	10.6 \pm 0.6	1.6 \pm 0.4	47.50 \pm 0.10	64(149)
22	60585.01	(0.500)	(3.100)	1.35 \pm 0.08	7.2 $^{+0.9}_{-1.0}$	0.82 $^{+0.05}_{-0.04}$	11.1 $^{+0.6}_{-0.7}$	1.9 \pm 0.4	42.90 \pm 0.10	84(148)
23	60585.85	(0.500)	3.0 $^{+4.0}_{-0.7}$	1.40 $^{+0.19}_{-0.12}$	5.8 $^{+1.2}_{-1.1}$	0.85 \pm 0.07	10.5 $^{+0.9}_{-0.7}$	3.4 $^{+1.8}_{-1.6}$	42.50 \pm 0.10	55(144)
24	60586.50	(0.500)	(3.100)	1.30 \pm 0.04	8.5 \pm 0.7	0.80 \pm 0.03	11.8 \pm 0.5	1.9 \pm 0.3	47.15 \pm 0.12	170(301)
25	60587.21	(0.500)	(3.100)	1.41 \pm 0.09	7.3 $^{+0.9}_{-1.0}$	0.85 $^{+0.06}_{-0.04}$	10.7 \pm 0.7	2.0 $^{+0.4}_{-0.5}$	48.90 \pm 0.12	86(147)
26	60588.44	(0.500)	(3.100)	1.34 \pm 0.09	7.8 $^{+1.0}_{-1.1}$	0.83 $^{+0.06}_{-0.04}$	10.9 \pm 0.7	2.0 \pm 0.4	45.90 \pm 0.11	95(149)
27	60593.41	(0.500)	2.7 $^{+2.9}_{-0.4}$	1.5 $^{+0.3}_{-0.2}$	6 $^{+3}_{-2}$	0.92 \pm 0.09	9.1 $^{+1.3}_{-0.7}$	2.0 \pm 0.5	44.10 \pm 0.13	78(134)
28	60599.45	(0.500)	3.3 $^{+0.3}_{-0.2}$	1.50 $^{+0.06}_{-0.03}$	4.4 $^{+0.2}_{-0.4}$	0.93 $^{+0.05}_{-0.04}$	8.9 $^{+1.0}_{-0.8}$	2.2 $^{+0.3}_{-0.2}$	35.31 \pm 0.04	298(309)
29	60616.90	(0.500)	(3.100)	1.19 \pm 0.03	3.15 $^{+0.12}_{-0.15}$	0.530 \pm 0.010	13.7 $^{+0.4}_{-0.6}$	-100 $^{+48}_{-20}$	5.50 \pm 0.02	308(259)
30	60618.51	(0.500)	1.950 \pm 0.013	(0.220)	60.8 $^{+7}_{-16}$	0.15 \pm 0.02	74 $^{+37}_{-14}$	-	2.420 \pm 0.010	87(127)
31	60621.09	(0.500)	2.03 \pm 0.02	0.34 \pm 0.02	18.7 $^{+1.0}_{-1.5}$	0.15 \pm 0.03	44 $^{+44}_{-10}$	-	0.950 \pm 0.005	107(119)
32	60622.19	(0.500)	2.21 \pm 0.03	0.350 \pm 0.010	13.5 \pm 0.5	-	-	-	0.511 \pm 0.004	93(89)
33	60623.15	(0.500)	2.09 \pm 0.05	0.33 \pm 0.01	12.0 $^{+0.7}_{-0.6}$	-	-	-	0.323 \pm 0.003	82(67)